Title page

Manuscript title

Prdm1 Positively Regulates Liver Type 1 ILCs Cancer Immune Surveillance and Preserves Functional Heterogeneity

Authors and affiliations

Jitian He[1], Le Gao[1], Peiying Wang[1], Wing Keung Chan[4], Yiran Zheng[1], Yumo Zhang[1], Jiming Wang[5], Huaiyong Chen[3,6,7], Zhouxin Yang[2], Youwei Wang[1]

[1]Institute of Medical Engineering & Translational Medicine, Tianjin University, Tianjin 300072, China.

[2]Zhejiang Provincial Key Lab of Geriatrics and Geriatrics Institute of Zhejiang Province, Zhejiang Hospital, Hangzhou 310030, China.

[3]College of Pulmonary and Critical Care Medicine, 8th Medical Center, Chinese PLA General Hospital, Beijing, China

[4]Department of Internal Medicine, Division of Hematology, The Ohio State University, Columbus, OH 43210, USA.

[5]Tianjin Economic-Technological Development Area (TEDA) Hospital, Tianjin 300451, China

[6]Department of Basic Medicine, Haihe Hospital, Tianjin University, Tianjin 300350, China.

[7]Tianjin Key Laboratory of Lung Regenerative Medicine, Tianjin 300350, China.

Authorship notes: JH, LG, and PW contributed equally to this work.

Co-corresponding authors: Huaiyong Chen (huaiyong.chen@foxmail.com), Zhouxin Yang (yangzhouxin@hotmail.com), Youwei Wang (youwei.wang@tju.edu.cn)

Address correspondence to: Youwei Wang, Institute of Medical Engineering & Translational Medicine, Tianjin University, Tianjin 300072, China. Email: youwei.wang@tju.edu.cn. Or to Zhouxin Yang, Zhejiang Provincial Key Lab of Geriatrics and Geriatrics Institute of Zhejiang Province, Zhejiang Hospital, Hangzhou 310030, China. Email: yangzhouxin@hotmail.com. Or to Huaiyong Chen, Department of Basic Medicine, Haihe Hospital, Tianjin University, Tianjin 300350, China. Email: huaiyong.chen@foxmail.com.

Abstract

Liver Type 1 innate lymphoid cells (ILCs) comprise conventional natural killer (cNK) cells and ILC1s. The main functions of Type 1 ILCs not only include directly killing target cells but also regulating the local immune microenvironment of the liver through the secretion of cytokines. Uncovering the intricate mechanisms by which transcriptional factors regulate and influence the functions of Type 1 ILCs, particularly within the context of liver tumors, presents a significant opportunity to amplify the effectiveness of immunotherapies against liver malignancies. Using Ncr1-drived conditional knockout mouse model, our study reveals the regulatory role of *Prdm1* in shaping the composition and maturation of liver Type 1 ILCs. Notably, Prdm1 regulates the ratio between NK cells and ILC1s, promoting a shift in the balance towards the direction of NK cells. Although *Prdm1* did not affect the killing function of cNK cells in an *in vivo* cytotoxicity model, a significant increase in cancer metastasis was observed in *Prdm1* knockout mice. IFN-γ, granzyme B, and perforin secretion decreased significantly in *Prdm1* deficient Type 1 ILCs. scRNA sequencing data also provided evidence that Prdm1 sustains functional subsets of liver type 1 ILCs and facilitates communications between Type 1 ILCs and macrophages. The present study unveiled a novel regulatory mechanism of Prdm1 in liver Type 1 ILCs, showing promising potential for developing innovative immune therapy strategies against liver cancer.

Main text

Introduction

Liver Type 1 ILCs consist of cNK cells and ILC1s (1), with distinct developmental trajectories and effect molecules (2). Both NK cells and ILC1s play indispensable roles in combatting viral infections (3), maintaining local immune homeostasis (4), eradicating malignant transformed cells (5), and fostering cross-talk with adaptive immunity (6). NK cells demonstrate potent cellular cytotoxicity, facilitating direct elimination of target cells (7). On the contrary, a defining attribute of ILC1s is their predominant cytokine-mediated functions, with limited cellular killing capacity (8). In a state of homeostasis, liver Type 1 ILCs ($CD45^{+}CD3^{-}NK1.1^{+}NKp46^{+}$) can be discriminated into cNK cells and ILC1s by the differential expression of CD49a and CD49b (1): liver cNK cells are marked by the expression of CD49b, while liver ILC1s exhibit a distinctive positivity for CD49a. Tumor Necrosis Factor Related Apoptosis Inducing Ligand (TRAIL) is also expressed on liver ILC1s, but not on liver NK cells (9, 10). Transcriptional factors (TFs) such as T-bet, Nfil3, PLZF, and ID2 are also required for Type 1 ILCs development or generation of their progenitors (11-14). Eomes is considered to be necessary for NK cell maturation, but not for ILC1s (15). On the contrary, deficiency of Hobit results in the depletion of ILC1s, while only leaving little impact on liver NK cells (16). These studies suggest that TFs may, or usually, play different roles in NK cells and ILC1s.

During the development of liver cancers, the functions of immune cells are often inhibited, resulting in the formation of an immunosuppressive tumor microenvironment, and sometimes even systemic immune suppression (17). Transforming a cold tumor into a hot tumor with a

72 stronger immune response is one of the goals of many cancer immunotherapies (18). Research
73 targeting the immune system is showing increasing clinical promise in liver cancer treatment (19).
74 Our recent study also found that Toll-like receptor agonists can significantly enhance the
75 anti-tumor effect of Sorafenib by reconstructing the tumor immune microenvironment and
76 reshaping the vascular system (20).

77 The anti-tumor activity of NK cells in the liver is relatively well-established, whereas the
78 relationship between ILC1 and tumors is still a topic of controversy. Clinical research findings
79 have shown that liver tumors with a higher infiltration of NK cells are associated with a better
80 prognosis (21). Decreased NK cell activity is closely correlated with the malignancy of liver
81 tumors and represents a significant risk factor for recurrence (22). The tumor microenvironment
82 orchestrates the transformation of NK cells into ILC1s in a TGF-β-dependent manner, resulting in
83 their diminished capacity to control tumor growth and metastasis. This process ultimately
84 promotes tumor immunoevasion (23). However, research has also revealed that, distinct from
85 directly inhibiting tumor growth, the primary function of ILC1 is to suppress the seeding of
86 metastatic tumor cells in liver tissue (5). Comprehensive research in this field is essential to
87 harness the precision of Type 1 ILCs targeted immunotherapy for liver cancers.

88 The transcription factor network governs the function of Type 1 ILCs and the balance
89 between NK and ILC1. Our research team, along with others, has observed that Smad4 promotes
90 the shift in balance from NK cells towards ILC1 in a TGF-beta-independent pathway. This study
91 also revealed that Smad4 positively regulates the expression of another transcription factor,
92 Prdm1(24, 25). PR domain 1 (Prdm1/Blimp1) plays a crucial role in the differentiation of B cells
93 into plasma cells and the homeostasis of T cells (26-28). The function and regulatory network of

94 Prdm1 in NK cells is distinct from B cells and T cells, for its expression is independent of B-cell
95 lymphoma 6 (Bcl-6) and Interferon Regulatory actor 4 (IRF4) but relies on T-bet. In the study that
96 identified Prdm1 as an essential transcriptional factor for NK cell maturation (29), no significant
97 differences were observed in IFN-γ production or cytotoxicity between Prdm1-deficient and
98 wild-type NK cells. Although Prdm1 expression is dependent on IL-15 in immature NK cells and
99 can be further upregulated by IL-12 or IL-21, it plays a role in downregulating the expression of
100 certain cytokine receptors, such as CD25, consequently diminishing the responsiveness of NK
101 cells to IL-2 (30). Notably, some studies have even suggested that Prdm1 suppresses the secretion
102 of IFN-γ by NK cells (31). These findings imply that, although Prdm1 promotes NK cell
103 development, it may function as a negative regulator of their activity. However, direct evidence
104 supporting the impact of Prdm1 on NK cell anti-tumor capabilities is still lacking. Furthermore,
105 there has been no investigation into its influence on the homeostasis of NK cells and ILC1s in the
106 liver, nor has there been an exploration of the underlying mechanisms.

107 In the current study, we found that the deletion of *Prdm1* in Ncr1^{+} cells resulted in an
108 imbalance in the homeostasis of liver Type 1 ILCs, with a shift towards cNK cells. The data also
109 support the essential role of Prdm1 in the cancer surveillance mediated by NK cells. While Prdm1
110 positively regulates genes associated with cellular cytotoxicity, it concurrently exerts inhibitory
111 control over certain positive regulators of NK cell development and functionality, such as JunB.
112 Using single-cell RNA sequencing, we have identified a subset of NK cells within the liver
113 characterized by elevated JunB expression. These cells exhibit decreased expression of genes
114 associated with cellular cytotoxicity, and their abundance significantly increases following Prdm1
115 knockout.

116

117 **Results**

118 ***Prdm1* promotes Type 1 ILCs homeostasis and terminal maturation**

119 Examination of 363 liver hepatocellular carcinoma (LIHC) patient samples from The Cancer
120 Genome Atlas (TCGA) revealed a positive correlation between the expression of NK
121 cell-associated genes (*NCR1*, *NCR3*, *KLRB1*, *CD160*, and *PRF1*) (32) and *PRDM1* expression
122 (Figure 1A). Patients with top and bottom quartiles of *NK-PRDM1* signature expression were
123 chosen for survival analysis (Figure 1B). Notably, patients with the *NK-PRDM1*^{hi} signature had
124 better overall survival compared to the these with NK-*PRDM1*^{lo} signature (Figure 1C). Similar
125 results were also found in skin cutaneous melanoma (SKCM, n=454) and lung adenocarcinoma
126 (LUAD, n=497) patients (Supplemental Figure 1, A-F). These data suggested that *PRDM1* in NK
127 cells might be essential for immune surveillance in some solid tumors, including liver cancer.
128 These findings prompted us to investigate the impact and mechanism of *PRDM1* in NK cells and
129 ILC1 within the context of liver cancer.

130 To achieve this, we developed a conditional knockout mouse model to specifically deplete
131 *Prdm1* in Type 1 ILCs. *Ncr1-Cre* mice were crossed with *Prdm1*$^{fl/fl}$ mice to generate *Ncr1-cre*
132 *Prdm1*$^{fl/fl}$ mice, which specifically knockout exons 6-8 of *Prdm1* (33) in NKp46 positive cells
133 (Figure 1D). The mice carrying *Ncr1*$^{Cre/+}$*Prdm1*$^{fl/fl}$ were referred to as *Prdm1*$^{\Delta Ncr1}$ mice, and the
134 mice carrying *Ncr1*$^{+/+}$*Prdm1*$^{fl/fl}$ were referred to as *Prdm1*$^{+/+}$ mice or wild-type (WT) mice. To
135 further validate the deletion of *Prdm1* in NKp46^{+} cells of *Prdm1*$^{\Delta Ncr1}$ mice, CD3^{-}NK1.1^{+}NKp46^{+}
136 cells were sorted and the expression of *Prdm1* was quantified by real-time RT-PCR. The

137 expression of *Prdm1* was almost undetectable in *Prdm1*$^{\Delta Ncr1}$ mice (Figure 1E), indicating
138 successful knockout of *Prdm1* in NKp46^{+} cells.

139 Proportion and absolute number of cNK cells in blood, bone marrow, lung, liver, spleen, and
140 lymph nodes were analyzed by flow cytometry. Compared with *Prdm1*$^{+/+}$ mice, the percentage of
141 cNK cells (CD3^{-}NK1.1^{+}NKp46^{+}) among lymphocytes was decreased in all of these tissues except
142 bone marrow and lymph nodes (Figure 1F; Supplemental Figure 2A). However, no significant
143 difference was observed in the percentage of cNK cells among bone marrow-derived lymphocytes
144 between *Prdm1*$^{\Delta Ncr1}$ and *Prdm1*$^{+/+}$ mice. The absolute number of cNK cells in blood, lung, liver,
145 and spleen also decreased in *Prdm1*$^{\Delta Ncr1}$ mice (Figure 1F; Supplemental Figure 2A). Only a slight
146 decrease in the number of cNK cells was observed in the lymph nodes of *Prdm1*$^{\Delta Ncr1}$ mice, which
147 did not reach statistical significance either (Supplemental Figure 2A). In contrast, the absolute
148 number of cNK cells in *Prdm1*$^{fl/fl}$ mice bone marrow is moderately higher than *Prdm1*$^{\Delta Ncr1}$ mice
149 (Figure 1F).

150 NK cell terminal maturation can be divided into four stages according to the expression of
151 CD11b and CD27 (34). Stage IV (CD11b^{+}CD27^{-}) NK cells show higher level of effector
152 molecules than any other stages and are considered as the most mature NK cells (35). Based on
153 the expression of CD11b and CD27, the maturation of cNK cells from blood, bone marrow, lung,
154 liver, spleen, and lymph nodes were assessed. Compared with *Prdm1*$^{+/+}$ mice, the proportion of
155 most mature CD11b^{+}CD27^{-} NK cells were significantly decreased in all of the analyzed tissues in
156 *Prdm1*$^{\Delta Ncr1}$ mice, without any exceptions (Figure 1G; Supplemental Figure 2B). Remarkably, an
157 increase in immature CD11b^{-}CD27^{+} NK cells was also observed in these tissues. Killer cell
158 lectin-like receptor subfamily G member 1 (KLRG1) is a lectin-like receptor which was

159 considered as another marker of NK cell maturation (36). In both *Prdm1*$^{+/+}$ and *Prdm1*$^{\Delta Ncr1}$ mice,
160 cNK cells from the liver and lung had the highest expression of KLRG1, following by blood and
161 spleen (Supplemental Figure 2, C and D). The lowest KLRG1 expression was observed in cNK
162 cells derived from lymph nodes and bone marrow, indicating the presence of the most immature
163 cNK cells in these tissues. Consistent with CD11b/CD27 based maturation analysis, a significant
164 loss of KLRG1^{+} NK cells in *Prdm1*$^{\Delta Ncr1}$ mice was observed compared to *Prdm1*$^{+/+}$ mice
165 (Supplemental Figure 2, C and D). Together, these data showed that *Prdm1* is required for the
166 terminal maturation of cNK cells among various tissues.

167 ***Prdm1* is required for Type 1 ILCs to control tumor metastasis**

168 Two subpopulations of liver Type 1 ILCs (gated by CD45^{+}CD3^{-}NK1.1^{+}NKp46^{+}) were further
169 analyzed based on the expression of CD49a and CD49b (Figure 2A). Compared with *Prdm1*$^{+/+}$
170 mice, the *Prdm1*$^{\Delta Ncr1}$ mice exhibited an increased percentage of cNK cells (CD49a^{-}CD49b^{+}) and
171 reduced proportion of ILC1s (CD49a^{+}CD49b^{-}) (Figure 2A). Of note, the absolute number of both
172 cNK cells and ILC1s were decreased in *Prdm1*$^{\Delta Ncr1}$ mice, with a more robustly reduction in ILC1s
173 (Figure 2A). This underscored the crucial role of *Prdm1* in maintaining the homeostasis of both
174 liver cNK cells and ILC1s.

175 The disruption of NK cell homeostasis and maturation due to *Prdm1* loss motivated us to
176 further explore whether deficiency of Prdm1 impaired NK cell cytotoxicity. A B2M-deficient
177 cell-based *in vivo* cytotoxicity assay was used to evaluate the effect of *Prdm1* on the cytotoxicity
178 of NK cells (37, 38). B2M-deficient cells do not have detectable Major Histocompatibility
179 Complex I (MHC-I) on the cell surface, making them the target of NK cells (39). Health NK cells

180 will reject B2M-deficient donor cells efficiently and the elimination was used to quantify the
181 cytotoxicity of NK cells. Although significant impaired homeostasis and maturation of NK cells
182 were observed in *Prdm1*$^{\Delta Ncr1}$ mice, no significant difference in the *in vivo* cytotoxicity assay were
183 observed between *Prdm1*$^{+/+}$ and *Prdm1*$^{\Delta Ncr1}$ mice (Figure 2, B and C).

184 While our B2M-deficient cell-based assay did not reveal a significant impact of *Prdm1* on
185 NK cell cytotoxicity, both our results and those of other researchers have demonstrated *Prdm1*'s
186 role in positively regulating NK cell development and homeostasis. Besides direct cytotoxicity,
187 other factors influence the anti-tumor capability of NK cells, such as the ability to counteract
188 tumor-induced immune suppression and exhaustion, the secretion of cytokines to activate other
189 immune cells for tumor elimination. Moreover, the cytotoxicity assay, due to its relatively short
190 duration, might not fully represent the anti-tumor activity of NK cells when continuously exposed
191 to immune inhibitory signals in the tumor microenvironment. Therefore, we initiated an *in vivo*
192 tumor model to further investigate the impact of *Prdm1* on NK cell anti-tumor capabilities.
193 B16F10 is a melanoma cell line with low expression of MHC-I, which was susceptible to NK cell
194 killing and usually used to evaluate NK cell anti-tumor capacity (40, 41). The B16F10 cells were
195 intravenously (for lung metastasis) or intrasplenic (for liver metastasis) administrated in the mice.
196 The melanoma nodes were quantified three (intravenous injection) or two (intrasplenic injection)
197 weeks after tumor inoculation. Compared with *Prdm1*$^{+/+}$ mice, deficiency of *Prdm1* resulted in
198 more metastasis nodules in both lung (~ 2-fold) and liver (~ 4-fold) (Figure 2, D and F).
199 Histological analysis further confirmed the increased frequency of metastasis tumor foci in
200 *Prdm1*$^{\Delta Ncr1}$ mice (Figure 2, E and G).

201 In agreement with our *in vivo* data, we also observed decreased IFN-γ secretion in *Prdm1*$^{\Delta Ncr1}$

202 mice-derived splenic cNK cells, liver cNK cells, and liver ILC1s when stimulated by IL-18 alone
203 or IL-12/IL-18 (Figure 2H; Supplemental Figure3), which indicated that *Prdm1* is required for full
204 activation of cNK cells and ILC1s in the context of IFN-γ production. These data implying that
205 although similar cellular killing capacity was observed between *Prdm1*$^{+/+}$ and *Prdm1*$^{\Delta Ncr1}$ mice,
206 *Prdm1* is indispensable for NK cell mediated tumor surveillance.

207 **Bulk RNA-seq depicts *Prdm1*-mediated functions in peripheral cNK cells**

208 Bulk RNA sequencing of splenic cNK cells (CD3$^-$NK1.1$^+$NKp46$^+$) was conducted to uncover
209 the molecular mechanisms by which *Prdm1* regulates NK cell anti-tumor immunity (Figure 3A).
210 Differentially expressed genes (DEGs) between *Prdm1*$^{+/+}$ and *Prdm1*$^{\Delta Ncr1}$ mice were determined
211 using a criterion of $\log_2$ (fold change) > 0.5 and $P < 0.05$. 445 DEGs were identified out of 17434
212 protein-coding genes, which consisted of 223 upregulated genes and 222 downregulated genes
213 (Figure 3B).

214 Gene Ontology (GO) analysis revealed the enrichment of glucuronate metabolism and
215 lymphocyte differentiation in upregulated genes in *Prdm1*$^{\Delta Ncr1}$ mice derived NK cells (Figure 3C),
216 both of which were associated with cellular growth and development. In contrast, leukocyte
217 mediate cytotoxicity, immune receptor activity, and integrin binding was enriched in the genes
218 which decreased their expression level in in *Prdm1*$^{\Delta Ncr1}$ mice (Figure 3C).

219 Gene Set Enrichment Analysis (GSEA) showed enriched NF-kappa B signaling pathway and
220 negative regulation of IL-6 production pathway in *Prdm1*-deficient cNK cells (Figure 3, D and E),
221 suggesting the potential targets by *Prdm1* to regulate NK cell function. Increased expression of
222 multiple TFs such as *Junb*, *Batf3*, *Nfkb1*, *Tcf7*, and *Nr4a2* was observed in *Prdm1* knockout cNK

223 cells, suggesting they might be suppressed by *Prdm1* (Figure 3F). Downregulation of granzyme B
224 (*Gzmb*), Perfroin (*Prf1*) were observed in *Prdm1* deficient NK cells (Figure 3F), implied
225 decreased anti-tumor ability, which was consistent with increased melanoma metastasis in
226 *Prdm1*$^{\Delta Ncr1}$ mice (Figure 2D and F). *Cxcr6*, and *Cx3cr1* were also decreased in the NK cells
227 derived from *Prdm1*$^{\Delta Ncr1}$ mice (Figure 3F), which was considered to play an important role in
228 promoting the egress of NK cells from bone marrow. This might be the reason for the quantity of
229 NK cells increased in bone marrow while decreasing in other peripheral tissues (Figure 1F). As a
230 result of the reduced expression levels of *Cxcr6* and *Cx3cr1*, NK cells were unable to egress from
231 the bone marrow and accumulated therein. Consistent with decreased production of IFN-γ after
232 stimulated by IL-12/IL-18 (Figure 2H), decreased expression of *Il18rap* and *Il12rb2* were
233 observed in *Prdm1*$^{\Delta Ncr1}$ cNK cells (Figure 3F), implying impaired response to cytokine
234 stimulation.

235 To confirm the result of RNA-sequencing, the expression of granzyme B and perforin were
236 also analyzed by flow cytometry. Lower granzyme B and perforin production was observed in
237 *Prdm1*-deficient splenic cNK cells, liver cNK cells and ILC1s (Figure 3, G and I; Supplemental
238 Figure 4, A and B). Notably, granzyme B decreased among all of the maturation stages of cNK
239 cells. Probably because of relatively low level of perforin in CD11b^{-}CD27^{+} and CD11b^{+}CD27^{+}
240 cNK cells, there is not statistical difference between *Prdm1*$^{+/+}$ and *Prdm1*$^{\Delta Ncr1}$ cNK cells. However,
241 significantly decrease in Perforin was observed in *Prdm1*$^{\Delta Ncr1}$ mice derived CD11b^{+}CD27^{-} NK
242 cells, which have the highest level of Perforin. (Figure 3, H and J; Supplemental Figure 4C).
243 These data implied that *Prdm1* directly regulates NK cells to exert cytotoxicity, not only due to the
244 less mature phenotype in *Prdm1*-deficient NK cells.

245 **scRNA-seq reveals unique properties of two clusters from liver type I ILCs following *Prdm1***
246 **knockout.**

247 To further investigate the effect of *Prdm1* in liver cNK cells and ILC1s, as well as the
248 changes in the haptic immune microenvironment caused by the deficiency of *Prdm1* in Type 1
249 ILCs, single-cell RNA sequencing (scRNA-seq) was performed for $CD45^+$ cells sorted from the
250 liver (Figure 3A; Supplemental Figure 5A). Initial quality control revealed high-quality of cell
251 purity, library assembly, and sequencing (Supplemental Figure 5B). 10978 cells passed the quality
252 criteria and were selected for further analysis (6161 from $Prdm1^{+/+}$ mice, 4,817 from $Prdm1^{\Delta Ncr1}$
253 mice). Unsupervised clustering of all sequenced cells based on transcript signatures identified
254 twelve distinct clusters, including B cells, Macrophages, $CD4^+$ T cells, $CD8^+$ T cells, dendritic
255 cells (DCs), NKT cells, cNK cells, ILC1s, Neutrophils, Monocytes, Basophils, and a small
256 number of undefined cells (Figure 4A). A higher percentage of Macrophages, $CD8^+$ T cells,
257 Monocytes, DCs, and a lower percentage of NK cells, ILC1s, $CD4^+$ T cells, and NKT cells was
258 observed in $Prdm1^{\Delta Ncr1}$ mice (Supplemental Figure 5C). Liver cNK cells and ILC1s were
259 identified based on the expression of surface markers and TFs (Supplemental Figure 5D). For
260 example, liver cNK cells expressed high levels of *Itga2* (CD49b) and Eomes, while ILC1s had
261 high levels expression of *Itga1* (CD49a) and *Tnfsf10* (Supplemental Figure 5E). In liver Type 1
262 ILCs, increased percentage of cNK cells and decreased percentage of ILC1s were observed in
263 $Prdm1^{\Delta Ncr1}$ mice (Figure 4, B and C), which was in line with the flow cytometry data (Figure 2A).

264 To better understand the specific function of *Prdm1* played in liver cNK cells and ILC1s, the
265 two subpopulations of liver Type 1 ILCs were further analyzed separately using unsupervised
266 clustering. Liver cNK cells and ILC1s were grouped into three clusters respectively and visualized

267 by Uniform Manifold Approximation and Projection (UMAP) (Figure 4, D-I). Based on the
268 cluster specific gene expression signature (Supplemental Figure 6, A and B), the subpopulation of
269 liver cNK cells were referred as "*Prf1*^{hi}", "*Junb*^{hi} ", and "*Cxcr3*^{hi}" cNK cells (Figure 4, D-F).

270 The *Prf1*^{hi} cNK cell cluster was defined by high expression of cytolysis-related genes,
271 including *Ncr1*, *Gzma*, *Gzmb*, *Prf1*, and *Fgl2* (Figure 4J; Supplemental Figure 6C), indicating the
272 strong target-killing ability of this cluster. GO analysis further revealed the enrichment signatures
273 of cytolysis, response to virus, and lymphocyte mediated immunity in the genes upregulated in
274 *Prf1*^{hi} cNK cell cluster, further confirming the cytotoxic effects of this cluster (Figure 4K). While
275 this cluster is present in both *Prdm1*$^{\Delta Ncr1}$ and *Prdm1*$^{+/+}$ mice, there is a significant reduction in
276 *Prdm1*$^{\Delta Ncr1}$ mice (Figure 4F). Additionally, both *Gzma* and *Gzmb* expression were downregulated
277 in *Prdm1*$^{\Delta Ncr1}$ mice derived cNK cells and ILC1s compared to those from *Prdm1*$^{+/+}$ mice (Figure
278 5A). These data underscore the crucial role of *Prdm1* in maintaining NK cells with immune
279 effector functions.

280 The *Junb*^{hi} liver cNK cell cluster distinguished themselves by higher expression of *Junb*
281 compared to other clusters (Figure 4J). The expression of *Junb* was also upregulated in *Prdm1*$^{\Delta Ncr1}$
282 derived cNK cells and ILC1s (Figure 5A). The predominant majority (92.98%) of *Junb*^{hi} liver
283 cNK cells are derived from *Prdm1*$^{\Delta Ncr1}$ mice, with less than ten percent (7.02%) originating from
284 *Prdm1*$^{+/+}$ mice (Figure 4F). Many signal transduction elements, gene expression regulator, and
285 transcriptional factors, such as *Nfkbia*, *Tnfaip3*, *Nr4a1/2/3*, *Batf3*, *Fos*, *Fosb*, *Tcf7*, and *Kit* were
286 upregulated in the *Junb*^{hi} liver cNK cells (Figure 4J; Supplemental Figure 6C). The expression of
287 cytotoxicity related genes, such as *Gzmb* and *Prf1*, in *Junb*^{hi} cluster was also lower than other cNK
288 cells (Figure 4J). GO analysis showed that the genes upregulated in *Junb*^{hi} liver cNK cells

289 enriched in cell differentiation, cell activation, and transcriptional regulation (Figure 4K). GSEA
290 indicates that the NF-kappa B, IL-17, MAPK, and TNF signaling pathways were upregulated in
291 this clusters (Figure 5, E-H). GSEA also showed that mitochondrial related pathways, such as
292 mitochondrial protein, oxidative phosphorylation, and respiratory electron transport chain were
293 suppressed in *Junb*^{hi} cNK cell cluster (Supplemental Figure 6, D-F). Increased proportion of
294 *Junb*^{hi} cluster in *Prdm1* deficient cNK cells suggested impaired anti-tumor activity, which was
295 consistent with more melanoma metastasis in *Prdm1*$^{\Delta Ncr1}$ mice and lower expression of
296 cytotoxicity-related genes in splenic cNK cells based on bulk RNA-sequencing.

297 The *Cxcr3*^{hi} cNK cell cluster was characterized with high expression of *Cxcr3*, *Ccr2*, and
298 some genes encoding ribosomal subunits such as *Rps7* (Supplemental Figure 6C). The enrichment
299 of chemokine receptors in the genes upregulated in the *Cxcr3*^{hi} cluster implying a greater
300 likelihood of them being tissue-resident compared with other cNK cell clusters (Figure 4K). The
301 significant enrichment of ribosomal subunits and cytoplasmic translation in *Cxcr3*^{hi} cluster (Figure
302 4K) revealed their distinct and active metabolic profile and the capability to mount immune
303 responses. The *Cxcr3*^{hi} cNK cell cluster had a remarkably decreased proportion in *Prdm1*$^{\Delta Ncr1}$
304 mice (Figure 4F), which emphasized the critical role of *Prdm1* in maintaining this cluster of liver
305 cNK cells. Consisting with the flow cytometry result that showed an increase in the number of NK
306 cells in the bone marrow and a decrease in NK cells in peripheral tissues, bulk RNA sequencing
307 data also found that the expression of *Cx3cr1* and *Cxcr6* decreased in *Prdm1*$^{\Delta Ncr1}$ cNK cells. These
308 findings supported the hypothesis that *Prdm1*, through regulating chemokine receptor expression
309 levels, influenced the distribution of NK cells in the bone marrow and peripheral tissues,
310 particularly within the liver tissue.

311 Three clusters of ILC1s were identified from liver ILC1s (Figure 4, G-I), comprising "*Il7r*^{hi}",
312 "*Klra*^{hi}", and "*Gzma*^{hi}" ILC1s. The first two clusters of ILC1s were characterized by higher
313 expression of *Il7r* (CD127) and *Klra5* separately, while the *Gzma*^{hi} ILC1 cluster was identified by
314 elevated expression of both *Gzma* and *Gzmb* (Supplemental Figure 7, A-C). The *Il7r*^{hi} ILC1s
315 cluster was distinguishable from other ILC1 clusters by its high expression of *Il7r*, IL18RA
316 (*Il18r1*), and IFN-γ (*Ifng*) (Figure 5B; Supplemental Figure 7C). The high expression of *Il18r1*
317 and *Ifng* in *Il7r*^{hi} ILC1s indicated this cluster of cells was highly responsive to IL-18. Module
318 scores, calculated based on the expression of feature genes within the *Junb*^{hi} cNK cell cluster,
319 revealed a comparable *Junb*^{hi} signature expression pattern within the *Il7r*^{hi} ILC1 cluster (Figure
320 5C). GO analysis and GSEA showed that IL-17, NF-kappa B, TNF, MAPK signaling pathway and
321 T cell differentiation were activated in the *Il7r*^{hi} ILC1 cluster (Figure 5D, I and J; Supplemental
322 Figure 7D-F). Considering the close relationship between IL-17 mediated immunity response and
323 ILC3 (42), it is plausible that the observed heterogeneity within this cluster may be attributed, at
324 least in part, to potential plasticity between ILC1 and ILC3 subsets. These two clusters appear
325 reminiscent of an intermediate stage in the conversion process from cNK cells to ILC1s, as
326 previously described (23, 43). There was no significant difference in the proportion of this cluster
327 between WT and in *Prdm1*$^{\Delta Ncr1}$ mice.

328 The second liver ILC1 cluster, characterized by high expression of Ly49E (*Klra5*) and Ly49G
329 (*Klra7*), was designated as the *Klra*^{hi} ILC1 cluster (Figure 5B). Notably, there was an elevated
330 proportion of *Klra*^{hi} ILC1s in *Prdm1*$^{\Delta Ncr1}$ ILC1s (39.7%) compared to *Prdm1*$^{+/+}$ ILC1s (28.1%).
331 Liver Ly49E^{+} ILC1s have been identified as possessing greater cytotoxic potential and a more
332 robust viral response compared to liver Ly49E^{-} ILC1s (44). The *Klra*^{hi} cluster exhibited notably

333 high expression of *Ccl5* (Supplemental Figure 7C). Previous research has underscored the pivotal
334 role of CCL5, produced by both cNK cells and ILC1s, in facilitating the accumulation of DCs
335 within the tumor microenvironment, thereby impeding tumor immune evasion, as highlighted in
336 studies (32, 45). The expression of *Ccl5* was reduced in the *Klra*^{hi} cluster of *Prdm1*$^{\Delta Ncr1}$ ILC1s
337 compared to *Prdm1*$^{+/+}$ ILC1s (Supplemental Figure 7C). This decrease in *Ccl5* expression could
338 potentially have a detrimental impact on the ability of *Klra*^{hi} ILC1s to develop a connection
339 between innate and adaptive immune responses.

340 The *Gzma*^{hi} ILC1 cluster was identified according to the high expression of *Gzma*, *Gzmb*, and
341 *Fgl2* (Supplemental Figure 7C), compared to other ILC1 clusters. GO analysis also revealed the
342 enrichment in cytolysis and stimulus-response capacity (Figure 5D) of the *Gzma*^{hi} ILC1 cluster.
343 Consistent with the *Prf1*^{hi} cNK cell cluster, the proportion of the *Gzma*^{hi} cluster among liver ILC1s
344 exhibited a considerable reduction in *Prdm1*$^{\Delta Ncr1}$ mice compared to *Prdm1*$^{+/+}$ mice, and the
345 expression of *Gzma* also downregulated in *Prdm1*$^{\Delta Ncr1}$ mice (Figure 5B). Previous reports showed
346 that GzmA^{+} ILC1 constituted the main population of liver ILC1s at birth, with the potential
347 target-killing ability (46, 47).

348 ***Prdm1* facilitates the intercellular communication between liver Type 1 ILCs and**
349 **macrophages**

350 The reciprocal crosstalk between Type 1 ILCs and macrophages plays a critical role in
351 maintaining liver immune homeostasis and anti-cancer immune surveillance. Based on the
352 scRNA-seq data, four clusters were generated from liver macrophages according to the
353 transcriptional profile. They were labeled as "*Ly6c2*^{hi}"; "*Cxcl2*^{hi}"; "*Ear2*^{hi}"; and "*C1q*^{hi}"

354 macrophages (Mac) (Figure 6A, Supplemental Figure 8, A-D).

355 High-resolution interactions among liver cNK cells, ILC1s, and macrophages were
356 established and compared between *Prdm1*$^{+/+}$ and *Prdm1*$^{\Delta Ncr1}$ mice using the CellChat program
357 (48). Interactions between ILC1s and macrophages were higher than that between cNK cells and
358 macrophages (Supplemental Figure 9, A and B). There is a significant decrease in the interaction
359 number between liver Type 1 ILCs (including cNK cells and ILC1s) and macrophages (~2 fold) in
360 *Prdm1*$^{\Delta Ncr1}$ mice (Figure 6, B and C). A reduction in the interaction of ligand-receptor, such as
361 Mif-CD74, Cxcl16-Cxcr6, and Cxcl10-Cxcr3 was observed in *Prdm1*$^{\Delta Ncr1}$ mice compared to
362 *Prdm1*$^{+/+}$ mice (Supplemental Figure 10). Liver cNK cells and ILC1s contributed equally to
363 macrophages through most pathways, while CXC chemokine ligand (CXCL), Thy-1 cell surface
364 antigen (THY1), and C-type lectin (CLEC) pathways participated more in ILC1-Mac interaction
365 than cNK-Macrophage interaction (Supplemental Figure 9, C and D). Compared to *Prdm1*$^{+/+}$ mice,
366 the information flow of CXCL and macrophage migration inhibitory factor (MIF) pathways
367 significantly decreased in *Prdm1*$^{\Delta Ncr1}$ mice (Figure 6, D and E). These pathways play a crucial role
368 in facilitating macrophage migration. The pathway Thrombospondin (THBS) was upregulated in
369 *Prdm1*$^{\Delta Ncr1}$, which was consistent with the higher expression of *Thbs1* in *Prdm1*$^{\Delta Ncr1}$ macrophages
370 (Supplemental Figure 8C). The CXCL signaling was sent from *Cxcl2*^{hi} macrophage and *C1q*^{hi}
371 macrophage, targeting all ILC1 clusters and *Cxcr3*^{hi} cNK cell clusters (Figure 6F). Of note,
372 although the population of *Cxcl2*^{hi} macrophage primarily comprised cells from *Prdm1*$^{\Delta Ncr1}$ mice,
373 the interaction within the CXCL pathway between macrophages and Type 1 ILCs was only
374 observed in *Prdm1*$^{+/+}$ sample (Figure 6F). These changes could be linked to a decreased
375 population of ILC1s and *Cxcr3*^{hi} cNK cell cluster in *Prdm1*$^{\Delta Ncr1}$ mice, implying that the

376 homeostasis of *Cxcl2*^{hi} macrophages required sufficient signals from cNK cells and ILC1s. The
377 impaired CXCL-CXCR interactions might subsequently lead to reduced recruitment and
378 activation of Type 1 ILCs and macrophages within the tumor microenvironment.

379 ***Prdm1* safeguards Type 1 ILCs from exhaustion-like phenotypes in the tumor**
380 **microenvironment**

381 The suppression of mitochondrial related pathways in *Junb*^{hi} cNK cell cluster, along with a
382 significant increase of this cNK cell cluster in *Prdm1*$^{\Delta Ncr1}$ mice, encouraged us to explore
383 mitochondrial function through flow cytometry. MitoTracker, MitoSOX, and
384 Tetramethylrhodamine methyl ester (TMRM) were used to assess the mitochondrial mass,
385 superoxide production, and mitochondrial membrane potential. A substantial decrease in mean
386 fluorescent intensities (MFIs) of MitoTracker was observed in *Prdm1*$^{\Delta Ncr1}$ splenic cNK cells, liver
387 cNK cells, and liver ILC1s when compared to their *Prdm1*$^{+/+}$ counterparts (Figure 6A). This
388 observation aligns with the enrichment of downregulated genes from *Prdm1* deficient sample in
389 mitochondrial related pathway, as revealed by RNA sequencing data (Supplemental Figure 6, D-F).
390 There was no significant difference in MitoSOX and TMRM between *Prdm1*$^{\Delta Ncr1}$ and *Prdm1*$^{+/+}$
391 mice (Figure 7, B and C), which suggested that the ATP synthesize capacity was minimally
392 affected by *Prdm1*.

393 IFN-γ is a critical cytokine for NK cells mediated cancer surveillance(49, 50) and impaired
394 production of IFN-γ was considered as a key hallmark of exhausted NK cells (51, 52). To evaluate
395 the IFN-γ secreting capacity of liver cNK cells and ILC1s in tumor microenvironment, B16F10
396 tumor cells were inoculated to the liver via splenic injection and the IFN-γ levels in response to

397 stimulation of IL-12 and/or IL-18 were assessed by flow cytometry (Supplemental Figure 11).
398 Compared with *Prdm1*$^{+/+}$, significant deceased of IFN-γ were observed in *Prdm1*$^{\Delta Ncr1}$ liver cNK
399 cells and ILC1s under the combinate stimulation of IL-12/IL-18 (Figure 7D), which was more
400 remarkable in liver ILC1s. Similar trends were observed when IL-12 or IL-18 was used alone,
401 although only liver ILC1s showed a significant decrease in response to IL-18 stimulation (Figure
402 7D). These findings were consistent with the heavy tumor burden observed in *Prdm1*$^{\Delta Ncr1}$ mice.

403 **Discussion**

404 Using Ncr1-driven conditional knockout transgenic mice, which specifically delete *Prdm1* in
405 Type 1 ILCs, we not only validated *Prdm1*'s positive regulation of NK cell maturation, but also
406 demonstrated its indispensable role in NK cell anti-tumor activity. The compromised
407 mitochondrial function and reduced IFN-γ, granzyme B, and perforin production appear to be
408 potential contributing factors to Prdm1-mediated cancer surveillance. Decreased expression of
409 *Cx3cr1* and *Cxcr6* was observed in *Prdm1*$^{\Delta Ncr1}$ splenic cNK cells (Figure 3F), both of which are
410 essential for NK cells egressing from bone marrow (53, 54). The quantity of cNK cells increased
411 exclusively in the bone marrow, with reductions observed in all other tissues (Figure 1F). This
412 indicated that *Prdm1* might regulate chemokine receptors to facilitate the egression of cNK cells
413 from the bone marrow to peripheral tissues. In addition, higher expression of *Cxcr6* compared to
414 cNK cells is also a key factor for liver tissue residence of ILC1s (55). Decreased expression of
415 *Cxcr6* in *Prdm1* deficient Type 1 ILCs may also contribute to the balance shift towards cNK cells.
416 scRNA sequencing analysis reveals that both liver cNK cells and ILC1s can be further
417 divided into three subgroups based on their gene expression patterns. Within the cNK cells, the

418 abundance of *Junb*^{hi} cluster substantially increased in *Prdm1*$^{\Delta Ncr1}$ mice (75.8%). Notably, these
419 cells account for less than 5% of WT cNK cells. High *Junb* expression stood out as a prominent
420 feature of this subgroup. Junb is a crucial transcriptional factor for the cytotoxic function of CD8^{+}
421 T cells and NK cells. However, excessive *Junb* expression has been found to promote T cell
422 exhaustion (56). Our previous study showed that as NK cells mature, the expression level of
423 *Prdm1* increased while the expression level of *Junb* gradually decreased (57). Our data
424 demonstrated that in NK cells, the expression level of *Junb* significantly increases upon the
425 deletion of Prdm1, indicating that *Junb* expression is suppressed by Prdm1. As *Junb* expression
426 decreases with NK cell maturation, and it is inhibited by the gradually increasing Prdm1 during
427 maturation. This implies that constraining *Junb* expression is likely a fundamental prerequisite for
428 NK cell maturation. However, the precise mechanism by which Prdm1 downregulates *Junb* in NK
429 cells still needs further research. Furthermore, *Junb*^{hi} NK cells exhibit lower expression levels of
430 cytotoxic genes and reduced mitochondrial-related signaling pathways. Mitochondrial
431 fragmentation has also been confirmed to be closely associated with NK cell exhaustion(58).
432 While our current data is not sufficient to definitively classify these cells as exhausted NK cells, it
433 supports that this particular group of NK cells demonstrates an exhausted phenotype. The
434 significant increase in this cell population following *Prdm1* knockout in NK cells may potentially
435 be one of the reasons why *Prdm1*$^{\Delta Ncr1}$ mice lose their tumor-killing capacity.

436 Our scRNA-seq data revealed that *Prdm1* plays distinct roles in regulating cNK cells and
437 ILC1s despite being required for both lineages. Specifically, *Prdm1* appears to be more involved
438 in promoting the resistance against exhaustion in cNK cells, whereas in ILC1s, it may play a role
439 in the plasticity between ILC1s and ILC3s. In both our previous study and a study by Colonna et

440 al. (57, 59), it was demonstrated that *Smad4*, a transcriptional factor involved in TGF-β signal
441 pathway, upregulated *Prdm1* in NK cells and depletion of *Smad4* resulted in a decreased ratio of
442 NK cells to ILC1s in the liver. However, knocking out *Prdm1* in Ncr1^{+} cells increased the ratio of
443 NK cells to ILC1s in liver type 1 ILCs (Figure 2A). These findings suggest the possibility of a
444 Smad4-independent pathway through which *Prdm1* promotes the maintenance of ILC1s, or that
445 *Prdm1* plays a more significant role in maintaining ILC1s compared to its role in NK cells.

446 Chronic inflammation is a crucial factor in promoting tumorigenesis, and macrophages play a
447 significant role in this process. Macrophages interact with both cNK cells and ILC1s. However,
448 the TFs that regulate these interactions are poorly understood. Fortunately, recent advances in
449 scRNA-seq technology and the CellChat software tool (48) have allowed us to gain a better
450 understanding of the *Prdm1* signaling pathway in Type 1 ILCs and its impact on macrophage
451 function at the transcriptional level. It is worth noting that normal ILC1-macrophage interactions
452 are more prevalent than those with NK cells (Supplemental Figure 9, A and B). Moreover, the
453 finding of increased liver metastasis in *Prdm1*$^{\Delta Ncr1}$ mice indicated the crucial role of *Prdm1* in
454 maintaining homeostasis between Type 1 ILCs and macrophages. Specifically, *Prdm1* may be
455 critical in preventing the overactivation of macrophages that can lead to cancer development.

456 **Methods**

457 **Mice**

458 *Prdm1*$^{fl/fl}$ mice were purchased from The Jackson Laboratory. *Ncr1-iCre* and *B2m*$^{-/-}$ mice
459 were purchased from Shanghai Model Organisms Center, Inc.. Six- to twelve-week-old littermates
460 were used for the experiment.

461 **Experimental metastasis model**

462 For lung metastasis model, 0.3 × 10^6 B16F10 cells were intravenous injected into mice.
463 Three weeks later, mice were euthanized for analysis. For liver metastasis model, mice were
464 inoculation with 0.5 × 10^6 B16F10 via intrasplenic injection. Three weeks later, mice were
465 euthanized for analysis. Lung and liver from tumor-bearing mice were fixed in 10% formalin and
466 embedded in paraffin. Sections were stained with H&E.

467 ***In vivo* cytotoxicity assay**

468 Donor splenocytes harvested from B2m deficient (*B2m*$^{-/-}$) mice were labeled with 5 μM
469 CFDA-SE. Donor splenocytes harvested from B2m-adequate (*B2m*$^{+/+}$) mice were labeled with 5
470 μM eF670. Labeled splenocytes from two mouse strains were mixed in a 1:1 ratio, and 1 × 10^7
471 cells in total were injected i.v. into *Prdm1*$^{+/+}$ and *Prdm1*$^{\Delta Ncr1}$ mice. One day after administration,
472 spleen and liver cells were isolated from recipient mice, and the population of labeled cells was
473 analyzed by flow cytometry. Rejection % was quantified according to the following formula:
474 $[1-(\%B2m^{+/+}/\%B2m^{-/-})_{Prdm1^{+/+}\text{ or }Prdm1^{\Delta Ncr1}}]\times 100\%$.

475 **Flow cytometry**

476 Flow cytometry and cell sorting were performed with a Cytoflex S/SRT (Beckman Coulter).
477 Data were analyzed using FlowJo software. The following antibodies were used (all purchased
478 from BioLegend unless otherwise indicated): CD45-PE-Cy7 (catalog 103114, clone 30-F11);
479 CD3ε-PerCP-Cy5.5 (catalog 100327, clone 145-2C11); NK1.1-BV421 (catalog 108741, clone
480 PK136); CD335-AF647 (catalog 560755, clone 29A1.4, BD Bioscience); CD49a-PE (catalog

481 562115, clone Ha31/8, BD Bioscience); CD49b-FITC (catalog 108906, clone DX5);
482 CD27-BV510 (catalog 124229, clone LG.3A10); CD11b-AF700 (catalog 101222, clone M1/70);
483 KLRG1-APC (catalog 561620, clone 2F1, BD Bioscience); CD49a-BV421 (catalog 740046, clone
484 Ha31/8, BD Bioscience); IFN-γ-PE (catalog 505807, clone XMG1.2); Granzyme B (catalog
485 372207, clone QA16A02); Perforin (catalog 154305, clone S16009A); CD49b-APC-Cy7 (catalog
486 108919, clone DX5) ; IgG-PE (catalog 402203, clone 27-35); CD335-BV510 (catalog 137623,
487 clone 29A1.4); TIGIT-PE (catalog 622205, clone A17200C); CD3ε-APC-Cy7 (catalog 100330,
488 clone 145-2C11). For mitochondrial metabolic assay, fresh cells were incubated in 37°C media for
489 30min with 100 nM MitoTracker Green (catalog M7514, Invitrogen), 100 nM TMRM (catalog
490 T668; Invitrogen), and 10 uM MitoSOX Red (catalog M36008; Invitrogen), respectively.
491 Surface-stained after washing with PBS and then detected by flow cytometry. For intracellular
492 IFN-γ staining, Cells freshly obtained from liver and spleen were stimulated 12 hours with or
493 without cytokine. GolgiStop (BD Biosciences) was added 4 hours before intracellular staining.

494 **Bulk RNA sequencing**

495 Total RNA from FACS sorted splenic NK cells of *Prdm1*$^{+/+}$ and *Prdm1*$^{\Delta Ncr1}$ mice was
496 extracted by TRIzol reagent (Invitrogen), then reverse transcribed into cDNA. Library
497 construction was prepared using Illumina mRNA Library kit, and sequencing was performed by
498 the BGISEQ-500. Standard methods were used to analyze the RNA-seq data, including aligning
499 the reads to the genome by HISAT2 (v2.1.0) (60), and gene expression values (Counts) were
500 calculated using RSEM (v1.3.1) (61). DEGs were identified using DEseq2 (v1.4.5) (62) with a
501 cutoff of $\log_2$(fold change) > 0.5 and P < 0.05. The “clusterProfiler” package (v4.4.4) (63) and

502 gene sets from molecular signatures database (MSigDB) were used for GSEA and GO analysis.
503 The heatmap was plotted using the "Pheatmap" package (v1.0.12).

504 **Single-cell RNA sequencing**

505 FACS-sorted liver CD45^{+} cells with more than 80% cell viability were used for library
506 preparation. Each sample contained cells from three *Prdm1*$^{+/+}$ or *Prdm1*$^{\Delta Ncr1}$ mice. Gel
507 Bead-in-Emulsions (GEMs) were generated using the 10X Genomics Chromium system, which
508 combinates Master Mix, Single Cell 3' v3.1 Gel Beads, and Partitioning Oil with single cells.
509 GEMs were mixed with cell lysate and reverse transcription reagent to produce full-length cDNA.
510 After incubation, the GEMs were broken, and recovered cDNA were amplified via PCR.
511 Fragmentation, End repair, A-tailing, and Adaptor Ligation were performed to obtain final
512 libraries, which contain P5 and P7 sequences. The 3' library was sequenced on Novaseq 6000 with
513 approximately 50k read pairs/cell sequencing depth. The "Seurat" R package (v4.2.0) (64) was
514 used for data analysis. Initial quality control was performed to filter out the low-quality cells and
515 cell doublets. Cells with 200-5500 expressed genes and no more than 10% mitochondrial genes
516 were considered for high-quality. Doublets were filtered with the "scDblFinder" Package (v1.10.0)
517 (65). After quality control, we totally recovered 6161 cells and 4817 cells from *Prdm1*$^{+/+}$ and
518 *Prdm1*$^{\Delta Ncr1}$ mice, respectively. Principal component analysis (PCA) was used for cluster analysis.
519 The first 15 PCs were picked for clustering and further visualized by UMAP. Clusters-specific
520 marker was defined using the "FindAllMarkers" function, and clusters were manually annotated
521 based on the top 30 or 15 markers. The "clusterProfiler" package and gene set from MSigDB were
522 used for GSEA and GO analysis. "CellChat" package (v1.4.0) (48) was utilized to predict the

523 cell-to-cell communication from scRNA-seq data.

524 **TCGA datasets assay**

525 The normalized gene expression and survival datasets of cancer patients collected in The
526 Cancer Genome Atlas (TCGA) were downloaded from UCSC Xena (http://xena.ucsc.edu/) (66).
527 The mean expression of NK cell-associated genes (*NCR1*, *NCR3*, *PRF1*, *KLRB1*, *CD160*) was
528 defined as NK signature according to the previous study (32). NK cell-associated genes, together
529 with *PRDM1*, constitute the *NK-PRDM1* signature in this study. The mean expression of per genes
530 was ordered from high-to-low and plotted by heatmap using the "Pheatmap" package. The overall
531 survival of patients in the high and low quartiles expression of *NK-PRDM1* signature was selected
532 for analysis. Kaplan-Meier curves were plotted by GraphPad Prism.

533 **Statistics**

534 For experiment results, two-tailed t tests were used to measure the continuous and normally
535 distributed between the two independent groups. Paired t-tests were used to determine the
536 statistical significance between two paired groups. Log-rank tests were used to compare the
537 overall survival distribution between the two groups of patients. A P value less than 0.05 was
538 considered significant and data were presented as mean±SEM.

539 **Study approval**

540 All animal experiments were approved by The Tianjin University Animal Care and Use
541 Committee (protocol 00000000202010100023). No human subjects were performed in this study.

542

Author contributions

Jitian He, and Youwei Wang designed experiments, performed experiments, analyzed the data and wrote the manuscript. Jitian He, Le Gao, Peiying Wang, Yiran Zheng, and Yumo Zhang performed experiments. Wing Keung Chan, Jiming Wang, Huaiyong Chen, and Zhouxin Yang analyzed the data, interpreted results and reviewed the manuscript.

Acknowledgments

This work was supported by The National Key Research and Development Program of China (2022YFF1202900), and The Zhejiang Provincial Natural Science Foundation of China (LY21H150002).

Declaration of interests

The authors have declared that no conflict of interest exists.

557 # References

558 1. Peng H, Jiang X, Chen Y, Sojka DK, Wei H, Gao X, et al. Liver-resident NK cells confer
559 adaptive immunity in skin-contact inflammation. *J Clin Invest.* 2013;123(4):1444-56.
560 2. Bai L, Vienne M, Tang L, Kerdiles Y, Etiennot M, Escaliere B, et al. Liver type 1 innate
561 lymphoid cells develop locally via an interferon-gamma-dependent loop. *Science.*
562 2021;371(6536).
563 3. Weizman OE, Adams NM, Schuster IS, Krishna C, Pritykin Y, Lau C, et al. ILC1 Confer Early
564 Host Protection at Initial Sites of Viral Infection. *Cell.* 2017;171(4):795-808 e12.
565 4. Schuster IS, Wikstrom ME, Brizard G, Coudert JD, Estcourt MJ, Manzur M, et al. TRAIL+
566 NK cells control CD4+ T cell responses during chronic viral infection to limit autoimmunity.
567 *Immunity.* 2014;41(4):646-56.
568 5. Ducimetiere L, Lucchiari G, Litscher G, Nater M, Heeb L, Nunez NG, et al. Conventional NK
569 cells and tissue-resident ILC1s join forces to control liver metastasis. *Proc Natl Acad Sci U S*
570 *A.* 2021;118(27).
571 6. Fumagalli V, Venzin V, Di Lucia P, Moalli F, Ficht X, Ambrosi G, et al. Group 1 ILCs regulate
572 T cell-mediated liver immunopathology by controlling local IL-2 availability. *Science*
573 *immunology.* 2022;7(68):eabi6112.
574 7. Kiessling R, Klein E, and Wigzell H. "Natural" killer cells in the mouse. I. Cytotoxic cells
575 with specificity for mouse Moloney leukemia cells. Specificity and distribution according to
576 genotype. *European journal of immunology.* 1975;5(2):112-7.
577 8. Nabekura T, Riggan L, Hildreth AD, O'Sullivan TE, and Shibuya A. Type 1 Innate Lymphoid
578 Cells Protect Mice from Acute Liver Injury via Interferon-gamma Secretion for Upregulating

579 Bcl-xL Expression in Hepatocytes. *Immunity.* 2020;52(1):96-108 e9.

580 9. Takeda K, Cretney E, Hayakawa Y, Ota T, Akiba H, Ogasawara K, et al. TRAIL identifies
581 immature natural killer cells in newborn mice and adult mouse liver. *Blood.*
582 2005;105(5):2082-9.

583 10. Takeda K, Hayakawa Y, Smyth MJ, Kayagaki N, Yamaguchi N, Kakuta S, et al. Involvement
584 of tumor necrosis factor-related apoptosis-inducing ligand in surveillance of tumor metastasis
585 by liver natural killer cells. *Nat Med.* 2001;7(1):94-100.

586 11. Townsend MJ, Weinmann AS, Matsuda JL, Salomon R, Farnham PJ, Biron CA, et al. T-bet
587 regulates the terminal maturation and homeostasis of NK and Valpha14i NKT cells. *Immunity.*
588 2004;20(4):477-94.

589 12. Yokota Y, Mansouri A, Mori S, Sugawara S, Adachi S, Nishikawa S, et al. Development of
590 peripheral lymphoid organs and natural killer cells depends on the helix-loop-helix inhibitor
591 Id2. *Nature.* 1999;397(6721):702-6.

592 13. Gascoyne DM, Long E, Veiga-Fernandes H, de Boer J, Williams O, Seddon B, et al. The basic
593 leucine zipper transcription factor E4BP4 is essential for natural killer cell development.
594 *Nature immunology.* 2009;10(10):1118-24.

595 14. Constantinides MG, McDonald BD, Verhoef PA, and Bendelac A. A committed precursor to
596 innate lymphoid cells. *Nature.* 2014;508(7496):397-401.

597 15. Gordon SM, Chaix J, Rupp LJ, Wu J, Madera S, Sun JC, et al. The transcription factors T-bet
598 and Eomes control key checkpoints of natural killer cell maturation. *Immunity.*
599 2012;36(1):55-67.

600 16. Mackay LK, Minnich M, Kragten NA, Liao Y, Nota B, Seillet C, et al. Hobit and Blimp1

601 instruct a universal transcriptional program of tissue residency in lymphocytes. *Science.*
602 2016;352(6284):459-63.
603 17. Lee JC, Green MD, Huppert LA, Chow C, Pierce RH, and Daud AI. The Liver-Immunity
604 Nexus and Cancer Immunotherapy. *Clin Cancer Res.* 2022;28(1):5-12.
605 18. Galon J, and Bruni D. Approaches to treat immune hot, altered and cold tumours with
606 combination immunotherapies. *Nature reviews Drug discovery.* 2019;18(3):197-218.
607 19. Ruff SM, Shannon AH, Beane JD, and Pawlik TM. Highlighting novel targets in
608 immunotherapy for liver cancer. *Expert review of gastroenterology & hepatology.*
609 2022;16(11-12):1029-41.
610 20. He Y, Zhan L, Shi J, Xiao M, Zuo R, Wang C, et al. The Combination of R848 with Sorafenib
611 Enhances Antitumor Effects by Reprogramming the Tumor Immune Microenvironment and
612 Facilitating Vascular Normalization in Hepatocellular Carcinoma. *Adv Sci (Weinh).*
613 2023:e2207650.
614 21. Nersesian S, Schwartz SL, Grantham SR, MacLean LK, Lee SN, Pugh-Toole M, et al. NK cell
615 infiltration is associated with improved overall survival in solid cancers: A systematic review
616 and meta-analysis. *Transl Oncol.* 2021;14(1):100930.
617 22. Lee HA, Goh HG, Lee YS, Jung YK, Kim JH, Yim HJ, et al. Natural killer cell activity is a
618 risk factor for the recurrence risk after curative treatment of hepatocellular carcinoma. *BMC*
619 *Gastroenterol.* 2021;21(1):258.
620 23. Gao Y, Souza-Fonseca-Guimaraes F, Bald T, Ng SS, Young A, Ngiow SF, et al. Tumor
621 immunoevasion by the conversion of effector NK cells into type 1 innate lymphoid cells. *Nat*
622 *Immunol.* 2017;18(9):1004-15.

623 24. Cortez VS, Ulland TK, Cervantes-Barragan L, Bando JK, Robinette ML, Wang Q, et al.
624 SMAD4 impedes the conversion of NK cells into ILC1-like cells by curtailing non-canonical
625 TGF-beta signaling. *Nature immunology.* 2017;18(9):995-1003.
626 25. Wang Y, Chu J, Yi P, Dong W, Saultz JN, Wang Y, et al. SMAD4 promotes
627 TGF-beta-independent NK cell homeostasis and maturation and antitumor immunity. *The*
628 *Journal of clinical investigation.* 2018.
629 26. Keller AD, and Maniatis T. Identification and characterization of a novel repressor of
630 beta-interferon gene expression. *Genes Dev.* 1991;5(5):868-79.
631 27. Kallies A, Hawkins ED, Belz GT, Metcalf D, Hommel M, Corcoran LM, et al. Transcriptional
632 repressor Blimp-1 is essential for T cell homeostasis and self-tolerance. *Nat Immunol.*
633 2006;7(5):466-74.
634 28. Martins GA, Cimmino L, Shapiro-Shelef M, Szabolcs M, Herron A, Magnusdottir E, et al.
635 Transcriptional repressor Blimp-1 regulates T cell homeostasis and function. *Nat Immunol.*
636 2006;7(5):457-65.
637 29. Kallies A, Carotta S, Huntington ND, Bernard NJ, Tarlinton DM, Smyth MJ, et al. A role for
638 Blimp1 in the transcriptional network controlling natural killer cell maturation. *Blood.*
639 2011;117(6):1869-79.
640 30. Akman B, Hu X, Liu X, Hatipoglu T, You H, Chan WC, et al. PRDM1 decreases sensitivity of
641 human NK cells to IL2-induced cell expansion by directly repressing CD25 (IL2RA). *Journal*
642 *of leukocyte biology.* 2021;109(5):901-14.
643 31. Smith MA, Maurin M, Cho HI, Becknell B, Freud AG, Yu J, et al. PRDM1/Blimp-1 controls
644 effector cytokine production in human NK cells. *J Immunol.* 2010;185(10):6058-67.

645 32. Bottcher JP, Bonavita E, Chakravarty P, Blees H, Cabeza-Cabrerizo M, Sammicheli S, et al.
646 NK Cells Stimulate Recruitment of cDC1 into the Tumor Microenvironment Promoting
647 Cancer Immune Control. *Cell.* 2018;172(5):1022-37 e14.
648 33. Shapiro-Shelef M, Lin K-I, McHeyzer-Williams LJ, Liao J, McHeyzer-Williams MG, and
649 Calame K. Blimp-1 Is Required for the Formation of Immunoglobulin Secreting Plasma Cells
650 and Pre-Plasma Memory B Cells. *Immunity.* 2003;19(4):607-20.
651 34. Hayakawa Y, and Smyth MJ. CD27 dissects mature NK cells into two subsets with distinct
652 responsiveness and migratory capacity. *J Immunol.* 2006;176(3):1517-24.
653 35. Chiossone L, Chaix J, Fuseri N, Roth C, Vivier E, and Walzer T. Maturation of mouse NK
654 cells is a 4-stage developmental program. *Blood.* 2009;113(22):5488-96.
655 36. Huntington ND, Tabarias H, Fairfax K, Brady J, Hayakawa Y, Degli-Esposti MA, et al. NK
656 cell maturation and peripheral homeostasis is associated with KLRG1 up-regulation. *J*
657 *Immunol.* 2007;178(8):4764-70.
658 37. Bix M, Liao NS, Zijlstra M, Loring J, Jaenisch R, and Raulet D. Rejection of class I
659 MHC-deficient haemopoietic cells by irradiated MHC-matched mice. *Nature.*
660 1991;349(6307):329-31.
661 38. Bern MD, Parikh BA, Yang L, Beckman DL, Poursine-Laurent J, and Yokoyama WM.
662 Inducible down-regulation of MHC class I results in natural killer cell tolerance. *The Journal*
663 *of experimental medicine.* 2019;216(1):99-116.
664 39. Karre K, Ljunggren HG, Piontek G, and Kiessling R. Selective rejection of H-2-deficient
665 lymphoma variants suggests alternative immune defence strategy. *Nature.*
666 1986;319(6055):675-8.

667 40. Viant C, Fenis A, Chicanne G, Payrastre B, Ugolini S, and Vivier E. SHP-1-mediated
668 inhibitory signals promote responsiveness and anti-tumour functions of natural killer cells.
669 *Nat Commun.* 2014;5:5108.
670 41. Cillo C, Dick JE, Ling V, and Hill RP. Generation of drug-resistant variants in metastatic B16
671 mouse melanoma cell lines. *Cancer Res.* 1987;47(10):2604-8.
672 42. Spits H, Artis D, Colonna M, Diefenbach A, Di Santo JP, Eberl G, et al. Innate lymphoid
673 cells--a proposal for uniform nomenclature. *Nat Rev Immunol.* 2013;13(2):145-9.
674 43. Park E, Patel S, Wang Q, Andhey P, Zaitsev K, Porter S, et al. Toxoplasma gondii infection
675 drives conversion of NK cells into ILC1-like cells. *Elife.* 2019;8.
676 44. Chen Y, Wang X, Hao X, Li B, Tao W, Zhu S, et al. Ly49E separates liver ILC1s into
677 embryo-derived and postnatal subsets with different functions. *J Exp Med.* 2022;219(5).
678 45. Kirchhammer N, Trefny MP, Natoli M, Brucher D, Smith SN, Werner F, et al. NK cells with
679 tissue-resident traits shape response to immunotherapy by inducing adaptive antitumor
680 immunity. *Sci Transl Med.* 2022;14(653):eabm9043.
681 46. Di Censo C, Marotel M, Mattiola I, Muller L, Scarno G, Pietropaolo G, et al. Granzyme A and
682 CD160 expression delineates ILC1 with graded functions in the mouse liver. *European*
683 *journal of immunology.* 2021;51(11):2568-75.
684 47. Friedrich C, Taggenbrock R, Doucet-Ladeveze R, Golda G, Moenius R, Arampatzi P, et al.
685 Effector differentiation downstream of lineage commitment in ILC1s is driven by Hobit across
686 tissues. *Nat Immunol.* 2021;22(10):1256-67.
687 48. Jin S, Guerrero-Juarez CF, Zhang L, Chang I, Ramos R, Kuan CH, et al. Inference and
688 analysis of cell-cell communication using CellChat. *Nat Commun.* 2021;12(1):1088.

689 49. Takeda K, Nakayama M, Sakaki M, Hayakawa Y, Imawari M, Ogasawara K, et al.
690 IFN-gamma production by lung NK cells is critical for the natural resistance to pulmonary
691 metastasis of B16 melanoma in mice. *Journal of leukocyte biology.* 2011;90(4):777-85.
692 50. Lin Q, Rong L, Jia X, Li R, Yu B, Hu J, et al. IFN-gamma-dependent NK cell activation is
693 essential to metastasis suppression by engineered Salmonella. *Nature communications.*
694 2021;12(1):2537.
695 51. Roe K. NK-cell exhaustion, B-cell exhaustion and T-cell exhaustion-the differences and
696 similarities. *Immunology.* 2022;166(2):155-68.
697 52. Zhang Q, Bi J, Zheng X, Chen Y, Wang H, Wu W, et al. Blockade of the checkpoint receptor
698 TIGIT prevents NK cell exhaustion and elicits potent anti-tumor immunity. *Nature*
699 *Immunology.* 2018;19(7):723-32.
700 53. Sciume G, De Angelis G, Benigni G, Ponzetta A, Morrone S, Santoni A, et al. CX3CR1
701 expression defines 2 KLRG1+ mouse NK-cell subsets with distinct functional properties and
702 positioning in the bone marrow. *Blood.* 2011;117(17):4467-75.
703 54. Chea S, Possot C, Perchet T, Petit M, Cumano A, and Golub R. CXCR6 Expression Is
704 Important for Retention and Circulation of ILC Precursors. *Mediators Inflamm.*
705 2015;2015:368427.
706 55. Hudspeth K, Donadon M, Cimino M, Pontarini E, Tentorio P, Preti M, et al. Human
707 liver-resident CD56(bright)/CD16(neg) NK cells are retained within hepatic sinusoids via the
708 engagement of CCR5 and CXCR6 pathways. *J Autoimmun.* 2016;66:40-50.
709 56. Lynn RC, Weber EW, Sotillo E, Gennert D, Xu P, Good Z, et al. c-Jun overexpression in CAR
710 T cells induces exhaustion resistance. *Nature.* 2019;576(7786):293-300.

711 57. Wang Y, Chu J, Yi P, Dong W, Saultz J, Wang Y, et al. SMAD4 promotes
712 TGF-beta-independent NK cell homeostasis and maturation and antitumor immunity. *J Clin*
713 *Invest.* 2018;128(11):5123-36.
714 58. Zheng X, Qian Y, Fu B, Jiao D, Jiang Y, Chen P, et al. Mitochondrial fragmentation limits NK
715 cell-based tumor immunosurveillance. *Nature immunology.* 2019;20(12):1656-67.
716 59. Cheng HP, Huang CJ, Tsai ML, Ong HT, Cheong SK, Choo KB, et al. MicroRNA-362
717 negatively and positively regulates SMAD4 expression in TGF-beta/SMAD signaling to
718 suppress cell migration and invasion. *Int J Med Sci.* 2021;18(8):1798-809.
719 60. Kim D, Langmead B, and Salzberg SL. HISAT: a fast spliced aligner with low memory
720 requirements. *Nat Methods.* 2015;12(4):357-60.
721 61. Li B, and Dewey CN. RSEM: accurate transcript quantification from RNA-Seq data with or
722 without a reference genome. *BMC Bioinformatics.* 2011;12:323.
723 62. Love MI, Huber W, and Anders S. Moderated estimation of fold change and dispersion for
724 RNA-seq data with DESeq2. *Genome Biol.* 2014;15(12):550.
725 63. Wu T, Hu E, Xu S, Chen M, Guo P, Dai Z, et al. clusterProfiler 4.0: A universal enrichment
726 tool for interpreting omics data. *Innovation (Camb).* 2021;2(3):100141.
727 64. Hao Y, Hao S, Andersen-Nissen E, Mauck WM, 3rd, Zheng S, Butler A, et al. Integrated
728 analysis of multimodal single-cell data. *Cell.* 2021;184(13):3573-87 e29.
729 65. Germain PL, Lun A, Garcia Meixide C, Macnair W, and Robinson MD. Doublet identification
730 in single-cell sequencing data using scDblFinder. *F1000Res.* 2021;10:979.
731 66. Caicedo HH, Hashimoto DA, Caicedo JC, Pentland A, and Pisano GP. Overcoming barriers to
732 early disease intervention. *Nat Biotechnol.* 2020;38(6):669-73.
733

734 # Figures legends

735 **Figure 1. *Prdm1* promotes type 1 ILCs homeostasis and terminal maturation.**

736 (**A**) Correlation between the average expression of NK cell-associated genes(*NCR1*, *NCR3*, *PRF1*,
737 *CD160*, *KLRB1*) and *PRDM1* in LIHC (Liver Hepatocellular Carcinoma; n=363) patients sourced
738 from TCGA datasets. (**B**) Heatmap of the ordered, z-score normalized expression values for
739 *PRDM1* and NK cell-associated genes in liver cancer patients. The top and bottom quartiles of all
740 patient samples are indicated. (**C**) Prognostic value of the *NK-PRDM1* signature for overall
741 survival of liver cancer patients comparing high and low quartiles. (**D**) Schematic representation
742 of the Prdm1-conditional knockout mouse model. Targeted exon 6-8 of *Prdm1* (top) is flanked
743 with *loxP* sites (middle). Ncr1-expressed Cre recombinase was used to generate the $Prdm1^{\Delta Ncr1}$
744 allele (bottom). (**E**) Real-time RT-PCR quantification of *Prdm1* expression in $NKp46^{+}$ cells to
745 determine the presence of *Prdm1* (n=5). (**F**) Representative flow cytometric plots (left) and
746 quantification (right) of the proportion and absolute number of $CD3^{-}NKp46^{+}$ cells among
747 lymphocytes in liver, lung, and bone marrow (n=8). (**G**) Representative flow cytometric plots (left)
748 of the CD11b and CD27 expression within $CD3^{-}NK1.1^{+}NKp46^{+}$ cells in liver, lung, and bone
749 marrow (n=7). Right panel showed the percentage of distinct stages of NK cells. Data are
750 presented as the mean±SEM and were analyzed by 2-tailed, paired t-test. Differences were
751 evaluated between littermates. Each circle and square on graphs represents an individual mouse; *P*,
752 *P*-value; r, pearson correlation coefficient; *, $P<0.05$; **, $P<0.01$, ns, not significant.

753 **Figure 2. *Prdm1* is required for type I ILCs to control tumor metastasis.**

754 (**A**) Representative flow cytometric plots (left) of liver cNK cells ($CD49a^{-}CD49b^{+}$) and ILC1s
755 ($CD49a^{+}CD49b^{-}$) from *Prdm1*$^{+/+}$ and *Prdm1*$^{\Delta Ncr1}$ mice. The two bar graghs (right) quantitate the
756 percentages and absolute numbers of cells respectively (n=7). (**B** and **C**) Splenocytes from *B2m*$^{-/-}$
757 and *B2m*$^{+/+}$ were labeled with CFDASE and eF670 respectively. Labeled cells were 1:1 mixed and
758 injected i.v. into *Prdm1*$^{+/+}$ and *Prdm1*$^{\Delta Ncr1}$ recipient mice to evaluate *in vivo* NK cell target-killing
759 ability. Representative flow cytometric plots (left) of transferred cells recovered from recipient
760 mice and percentage (right) of NK cell-specific rejection of donor cells in spleen (n=6) (**B**) and
761 liver (n=7) (**C**) between *Prdm1*$^{+/+}$ and *Prdm1*$^{\Delta Ncr1}$ mice. (**D** and **F**) Image (left) and quantification
762 (right) of tumor nodes on the livers (n=7) (**D**) and lungs (n=10) (**F**) of *Prdm1*$^{+/+}$ and *Prdm1*$^{\Delta Ncr1}$
763 mice at day 14 or 21 after inoculation with B16F10 melanoma cells. (**E** and **G**) Histopathological
764 images of liver (**E**) and lung (**G**) tissues stained by hematoxylin-eosin to detect tumor metastasis.
765 Red bar indicates 500 μm distance under the microscope. (**H**) Liver cells and splenocytes were
766 costimulated in the presence or absence of IL-12 and IL-18 for 12 hours. GolgiStop was added 4
767 hours before intracellular staining of IFN-γ. The graphs showed percentage of IFN-γ^{+} splenic cNK
768 cells, liver cNK cells and ILC1s from *Prdm1*$^{+/+}$ and *Prdm1*$^{\Delta Ncr1}$ mice (n=5). Data are presented as
769 the mean±SEM and were analyzed by 2-tailed, paired t-test. Differences were evaluated between
770 littermates. Each circle and square on graphs represents an individual mouse; *P*, *P*-value; *,
771 $P<0.05$; **, $P<0.01$, ns, not significant.

772 **Figure 3. Bulk RNA-seq depicts *Prdm1*-mediated functions in peripheral cNK cells.**

773 (**A**) Splenic cNK cells and liver $CD45^{+}$ cells were sorted from *Prdm1*$^{+/+}$ and *Prdm1*$^{\Delta Ncr1}$ mice

774 using flow cytometry, and prepared for bulk RNA-seq and single-cell RNA-seq analysis. (**B**)
775 Volcano plot of the bulk RNA-seq differentially expressed genes (log_2(fold change)>0.5; P<0.05)
776 in splenic cNK cells between *Prdm1*$^{+/+}$ and *Prdm1*$^{\Delta Ncr1}$ mice. Upregulated and downregulated
777 genes in *Prdm1*$^{\Delta Ncr1}$ cells were highlighted in red and blue. (**C**) Enriched Gene Ontology (GO)
778 terms of DEGs in *Prdm1*$^{\Delta Ncr1}$ cells compared *Prdm1*$^{+/+}$ cells. The Enrichment gene set in
779 upregulated (red) and downregulated (blue) genes were indicated in different colours. Bar length
780 represents statistical significance. (**D** and **E**) Gene Set Enrichment Analysis (GSEA) showing the
781 enrichment of negative regulation of IL-6 production (**D**) and NF-kappa B signaling pathway (**E**)
782 of DEGs in *Prdm1*$^{\Delta Ncr1}$ cells compared *Prdm1*$^{+/+}$ cells. NES, normalized enrichment score. (**F**)
783 Heatmap of selected genes from DEGs. Shown is z-score transformed expression of DEGs. (**G**
784 and **I**) Representative flow cytometric plots (left) and cumulative data (right) showing the relative
785 mean fluorescence intensities (MFIs) of Granzyme B (**G**) and Perforin (**I**) in liver cNK cells and
786 ILC1s from *Prdm1*$^{+/+}$ and *Prdm1*$^{\Delta Ncr1}$ mice (n=5). (**H** and **J**) Relative MFIs of Granzyme B (**H**)
787 and Perforin (**J**) in splenic NK cells at different stages of maturation was analyzed by flow
788 cytometry (n=5). Data are presented as the mean±SEM and were analyzed by 2-tailed, paired t-test.
789 Differences were evaluated between littermates. Each circle and square on graphs represents an
790 individual mouse; P, P-value; *, P<0.05; **, P<0.01, ns, not significant.

791 **Figure 4. scRNA-seq reveals unique properties of two clusters from liver type I ILCs**
792 **following *Prdm1* knockout.**

793 (**A**) Uniform manifold approximation and projection (UMAP) visualization of liver CD45$^+$ cells
794 from *Prdm1*$^{+/+}$ and *Prdm1*$^{\Delta Ncr1}$ mice. Twelve clusters were defined and indicated by distinct

795 colours. Each dot represents a single cell. (**B**) UMAP visualization of liver cNK and ILC1 clusters.
796 Cells were colored by origins (*Prdm1*$^{+/+}$-blue; *Prdm1*$^{\Delta Ncr1}$-red). (**C**) Percentages of cNK cells and
797 ILC1s in type I ILCs (left), and their distribution in each cluster (right). (**D-I**) UMAP visualization
798 of three different liver cNK (**D**) and ILC1 (**G**) clusters from two mouse strains (**E** and **H**).
799 Proportions of cNK cells (**F**) and ILC1s (**I**) among total cells (cNK cells or ILC1s) (left) and
800 within clusters (right) were calculated respectively. (**J**) Violin plots showing the normalized
801 expression of select genes in different cNK clusters. (**K**) Enriched GO term of marker genes in
802 three cNK clusters. Dot size represents enriched gene number, and color intensity represents
803 significance.

804 **Figure 5. *Junb*^{hi} signature is associated with the activation of multiple signaling pathways.**

805 (**A**) Ridge plots showing the normalized expression of *Gzmb, Prf1*, and *Junb* in cNK and ILC1
806 clusters between *Prdm1*$^{+/+}$ and *Prdm1*$^{\Delta Ncr1}$ cells. (**B**) Violin plots showing the normalized
807 expression of select genes in different ILC1 clusters. (**C**) Violin plot showing the *Junb*^{hi} signature
808 score for cNK cell and ILC1 clusters, calculated using the signature genes of *Junb*^{hi} cNK cluster.
809 (**D**) Enriched GO term of marker genes in three ILC1 clusters. Dot size represents enriched gene
810 number, and color intensity represents significance. (**E-J**) GSEA plots (left) depicting the
811 enrichment of NF-kappa B (**E**) , TNF (**F**) , IL-17 (**G**) , and MAPK (**H**) signaling pathway in *Junb*^{hi}
812 cNK cluster compared with clusters of *Prf1*^{hi} and *Cxcr3*^{hi} cNK cells, and the enrichment of IL-17
813 signaling pathway (**I**) and T cell differentiation (**J**) in *Il7r*^{hi} ILC1 cluster compared with clusters of
814 *Klra*^{hi} and *Gzma*^{hi} ILC1s. Right panel showed dynamic relative expression of the given gene sets
815 from cluster1 to cluster3 between *Prdm1*$^{+/+}$ and *Prdm1*$^{\Delta Ncr1}$. Dots represent the average expression

816 of given gene set in each cell, which was calculated through the sum of normalized expression of
817 each individual gene within the designated gene set in every single cell. NES, normalized
818 enrichment score.

819 **Figure 6. *Prdm1* facilitates the intercellular communication between liver type I ILCs and**
820 **macrophages.**

821 (**A**) UMAP visualization of macrophages (Mac) cluster. Four cell subsets were defined. (**B** and **C**)
822 Circle plots (**B**) and summary data (**C**) illustrating the significant enriched ligand–receptor pairs
823 among cluster of liver cNK cells, ILC1s, and macrophages from *Prdm1*$^{+/+}$ (left) and *Prdm1*$^{\Delta Ncr1}$
824 (right) cells. The thickness of the line indicates the number of enrich pairs, and the arrow reflects
825 the direction of the interaction. (**D**) Heatmap of overall signaling pattern recognized from
826 ligand-receptor pairs, which contained the sum of signaling from the sender and target cells. (**E**)
827 Bar graphs showing the information flow in selected active signaling patterns between *Prdm1*$^{+/+}$
828 and *Prdm1*$^{\Delta Ncr1}$ cells. Relative information flow was calculated as the sum of the communication
829 probability in given signaling patterns. (**F**) Chord plot of the CXCL signaling interaction network
830 among cluster of liver cNK cells, ILC1s, and macrophages in *Prdm1*$^{+/+}$ cells.

831 **Figure 7. *Prdm1* safeguards type I ILCs from exhaustion-like phenotypes in the tumor**
832 **microenvironment.**

833 (**A-C**) The Mitochondrial mass (MitoTracker Green staining; n=8) (**A**), Mitochondrial ROS
834 (MitoSOX staining; n=5) (B), and Mitochondrial membrane potential (TMRM staining; n=5) (**C**)
835 of splenic cNK cells, liver cNK cells and ILC1s were analyzed by flow cytometry. Representative
836 flow cytometric plots (left) and cumulative data (right) showing the relative mean fluorescence

837 intensities (MFIs) of each group. (**D**) Percentages of IFN-γ^+ liver cNK cells and ILC1s from
838 *Prdm1*$^{+/+}$ and *Prdm1*$^{\Delta Ncr1}$ tumor-bearing mice at day 14 after inoculation with B16F10 melanoma
839 cells via intrasplenic injection (n=5). Data are presented as the mean±SEM and were analyzed by
840 2-tailed, paired t-test. Differences were evaluated between littermates. Each circle and square on
841 graphs represents an individual mouse; *P*, *P*-value; *, *P*<0.05; **, *P*<0.01, ns, not significant.

842 **Supplemental Figure 1. High expression of *PRDM1-NK* signature predicts better overall**
843 **survival of cancer patients.**

844 (**A and D**) Correlation between the average expression of NK cell-associated genes(*NCR1*, *NCR3*,
845 *PRF1*, *CD160*, *KLRB1*) and *PRDM1* in skin cutaneous melanoma (SKCM, n=454) (**A**) and lung
846 adenocarcinoma (**D**) (LUAD, n=497) patients from TCGA datasets. (**B and E**) Heatmap of the
847 ordered, z-score normalized expression values for *PRDM1* and NK cell-associated genes in skin
848 cutaneous melanom (**B**) and lung cancer (**E**) patients. The top and bottom quartiles of all patient
849 samples are indicated. (**C and F**) Prognostic value of the *NK-PRDM1* signature for overall
850 survival of skin cutaneous melanom (**C**) and lung cancer (**F**) patients comparing high and low
851 quartiles. *P*, *P*-value; r, pearson correlation coefficient.

852 **Supplemental Figure 2. *Prdm1* plays an essential role in type I ILCs homeostasis and**
853 **maturation.**

854 (**A**) Representative flow cytometric plots (left) and quantification (right) of the proportion and
855 absolute number of CD3$^-$NKp46$^+$ cells among lymphocytes in blood, spleen, and lymph nodes
856 (n=8). (**B**) Representative flow cytometric plots (left) of the CD11b and CD27 expression within
857 CD3$^-$NK1.1$^+$NKp46$^+$ cells in blood, spleen, and lymph nodes (n=7). Right panel showed the

858 percentage of distinct stages of NK cells. **(C** and **D)** Representative flow cytometry analyses (**C**)
859 and quantification (**D**) of KLRG1 expression in $CD3^{-}NK1.1^{+}NKp46^{+}$ cells in blood, bone marrow,
860 lung, liver, spleen, and lymph nodes (n=5). Data are presented as the mean±SEM and were
861 analyzed by 2-tailed, paired t-test. Differences were evaluated between littermates. Each circle and
862 square on graphs represents an individual mouse; *P*, *P*-value; *, $P<0.05$; **, $P<0.01$, ns, not
863 significant.

864 **Supplemental Figure 3. *Prdm1* affects the IFN-γ secretion ability of type I ILCs.**

865 (**A**) Representative flow cytometric plot showing the frequency of IFN-γ^{+} cNK cells and ILC1s in
866 spleen and liver between *Prdm1*$^{+/+}$ and *Prdm1*$^{\Delta Ncr1}$ mice (n=5). Liver cells and splenocytes were
867 costimulated in the presence or absence of IL-12 and IL-18 for 12 hours. GolgiStop was added 4
868 hours before intracellular staining of IFN-γ. Data are presented as the mean±SEM and were
869 analyzed by 2-tailed, paired t-test. Differences were evaluated between littermates. Each circle and
870 square on graphs represents an individual mouse; *P*, *P*-value; *, $P<0.05$; **, $P<0.01$, ns, not
871 significant.

872 **Supplemental Figure 4. *Prdm1* deficiency impairs production of Granzyme B and Perforin in**
873 **type I ILC.**

874 (**A** and **B**) Representative flow cytometric plot (left) and summary data (right) showing the
875 relative mean fluorescence intensities (MFIs) of Granzyme B (**A**) and Perforin (**B**) in splenic NK
876 cells from *Prdm1*$^{+/+}$ and *Prdm1*$^{\Delta Ncr1}$ mice (n=5). (**C**) Splenic NK cells were divided into different
877 stages according to the expression of maturation markers CD11b and CD27. Representative flow
878 cytometric plot showing the MFIs of Granzyme B and Perforin in evaluated between littermates.

879 Data are presented as the mean±SEM and were analyzed by 2-tailed, paired t-test. Differences
880 were evaluated between littermates. Each circle and square on graphs represents an individual
881 mouse; *P*, *P*-value; r, pearson correlation coefficient; *, $P<0.05$; **, $P<0.01$, ns, not significant.

882 **Supplemental Figure 5. scRNA-seq identified subsets of liver CD45^{+} cell from *Prdm1*$^{+/+}$ and**
883 ***Prdm1*$^{\Delta Ncr1}$ mice.**

884 (**A**) Liver CD45^{+} cells from *Prdm1*$^{+/+}$ and *Prdm1*$^{\Delta Ncr1}$ mice were FACS-sorted for scRNA-seq. (**B**)
885 Quality control of the scRNA-seq data. Violin plot showing the nFeature_RNA, nCount_RNA,
886 and percentage of mitochondrial genes of sequencing cells. nFeature_RNA represents the number
887 of genes detected in each cell, and nCount_RNA represents the total number of molecules
888 detected within a cell. (**C**) Population of twelve liver CD45^{+} cell clusters between *Prdm1*$^{+/+}$ and
889 *Prdm1*$^{\Delta Ncr1}$ mice. (**D**) Dot plot showing the normalized expression of marker genes in liver cNK
890 cells and ILC1s clusters between *Prdm1*$^{+/+}$ and *Prdm1*$^{\Delta Ncr1}$. The dot size represents the percentage
891 of cells expressing selected genes, and color intensity represents the average expression. (**E**)
892 Violin plots showing the expression of marker genes *Itga2, Itga1, Eomes, and Tnfsf10* between
893 liver cNK cells and ILC1s between *Prdm1*$^{+/+}$ and *Prdm1*$^{\Delta Ncr1}$ mice.

894 **Supplemental Figure 6. Cluster-specific markers of liver cNK cell clusters.**

895 (**A**) Heatmap showing the expression of top 30 upregulated DEGs by log fold change (computed
896 using Wilcox test in the "FindAllMarkers" function of Seurat, avg_log2FC>0.25; P<0.05), across
897 the three liver cNK cell clusters (*Prf1*^{hi} cNK, *Junb*^{hi} cNK, *Cxcr3*^{hi} cNK) within *Prdm1*$^{+/+}$ and
898 *Prdm1*$^{\Delta Ncr1}$ mice. (**B**) Feature plots showing the normalized expression of selected markers for
899 liver cNK cell populations. (**C**) Violin plots showing the normalized expression of DEGs for each

900 cNK cluster within *Prdm1*$^{+/+}$ and *Prdm1*$^{\Delta Ncr1}$ mice. (**D-F**) GSEA of the enrichment of
901 Mitochondrial protein (**D**), Oxidative phosphorylation (**E**), and Respiratory electron transport
902 chain (**F**) in *Junb*^{hi} cNK cluster compared with clusters of *Prf1*^{hi} and *Cxcr3*^{hi} cNK cells. NES,
903 normalized enrichment score.

904 **Supplemental Figure 7. Cluster-specific markers of liver ILC1 clusters.**

905 (**A**) Heatmap showing the expression of top 30 upregulated DEGs by log fold change (computed
906 using Wilcox test in the "FindAllMarkers" function of Seurat, avg_log2FC>0.25; P<0.05), across
907 the three ILC1 clusters (*Il7r*^{hi} ILC1, *Klra*^{hi} ILC1, *Gzma*^{hi} ILC1) within *Prdm1*$^{+/+}$ and *Prdm1*$^{\Delta Ncr1}$
908 mice. (**B**) Feature plots showing the normalized expression of selected markers for liver ILC1
909 populations. (**C**) Normalized expression of DEGs for each ILC1 cluster within *Prdm1*$^{+/+}$ and
910 *Prdm1*$^{\Delta Ncr1}$ mice. (D) GSEA plots (left) depicting the enrichment of NF-kappa B (**D**) , TNF (**E**),
911 and MAPK (**F**) signaling pathways) in *Il7r*^{hi} ILC1 cluster compared with clusters of *Klra*^{hi} and
912 *Gzma*^{hi} ILC1s. Right panel showed dynamic relative expression of the given gene sets from
913 cluster1 to cluster3 between *Prdm1*$^{+/+}$ and *Prdm1*$^{\Delta Ncr1}$. Dots represent the average expression of
914 given gene set in each cell, which was calculated through the sum of normalized expression of
915 each individual gene within the designated gene set in every single cell. NES, normalized
916 enrichment score.

917 **Supplemental Figure 8. Identification of four distinct macrophage clusters.**

918 (**A**) Heatmap showing the top 15 upregulated DEGs across four macrophage clusters (computed
919 using Wilcox test in the "FindAllMarkers" function of Seurat, avg_log2FC>0.25; P<0.05). (**B**)
920 Percentage of macrophages from *Prdm1*$^{+/+}$ and *Prdm1*$^{\Delta Ncr1}$ mice among total cells (left) and

921 within clusters (right). (**C**) Violin plots showing the expression of selected markers of each
922 macrophage cluster within *Prdm1*$^{+/+}$ and *Prdm1*$^{\Delta Ncr1}$ mice. (**D**) GO analysis of four distinct
923 macrophage clusters. Dot size represents enriched gene number, and color intensity represents
924 significance.

925 **Supplemental Figure 9. Cell-Cell communication between cNK cells-macrophages and**
926 **ILC1s-macrophages.**

927 (**A and B**) Circle plots (**A**) and cumulative data (**B**) showing the interaction numbers between
928 cNK cells-macrophages and ILC1s-macrophages. The thickness of the line indicates the number
929 of enrich pairs, and the arrow reflects the direction of the interaction. (**C**) Heatmap of overall
930 signaling pattern recognized from ligand-receptor pairs between cNK cells-macrophages and
931 ILC1s-macrophages, which contained the sum of signaling from the sender and target cells. (**D**)
932 Bar graphs showing the information flow in selected active signaling patterns between cNK
933 cells-macrophages and ILC1s-macrophages. Relative information flow was calculated as the sum
934 of the communication probability in given signaling patterns.

935 **Supplemental Figure 10. Ligand-receptor interaction between type I ILCs and macrophages.**

936 Bubble plots showing the significant ligand-receptor pairs between cNK cells, ILC1s, and
937 macrophages within *Prdm1*$^{+/+}$ and *Prdm1*$^{\Delta Ncr1}$ mice. The highlighted Mif-Cd74 and Cxcl-Cxcr
938 signaling was significantly decreased in *Prdm1*$^{\Delta Ncr1}$ mice. Dot size represents the *P*-value, and
939 color intensity represents the communication probabilities. Empty space indicates a
940 communication probability of zero. *P*-value were calculated by the one-sided permutation test.

941 **Supplemental Figure 11: *Prdm1* maintains the IFN-γ production of liver type 1 ILCs in**

942 **tumor microenvironment.**

943 Representative flow cytometric plot of the frequency of IFN-γ^+ liver cNK cells and ILC1s from

944 *Prdm1*$^{+/+}$ and *Prdm1*$^{\Delta Ncr1}$ tumor-bearing mice at day 14 after inoculation with B16F10 melanoma

945 cells via intrasplenic injection (n=5). Data are presented as the mean±SEM and were analyzed by

946 2-tailed, paired t-test. Differences were evaluated between littermates. Each circle and square on

947 graphs represents an individual mouse; *P*, *P*-value; *, $P<0.05$; **, $P<0.01$, ns, not significant.

948

Graphical abstract

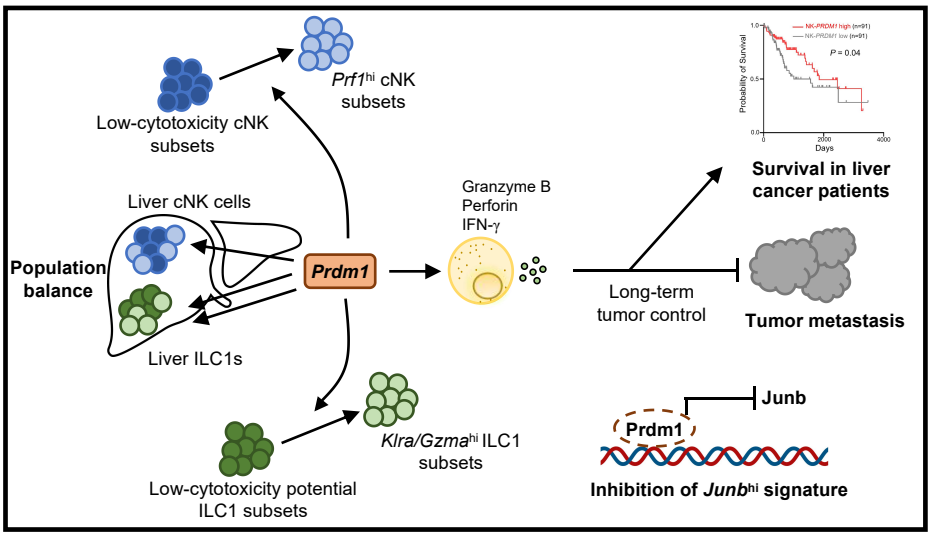

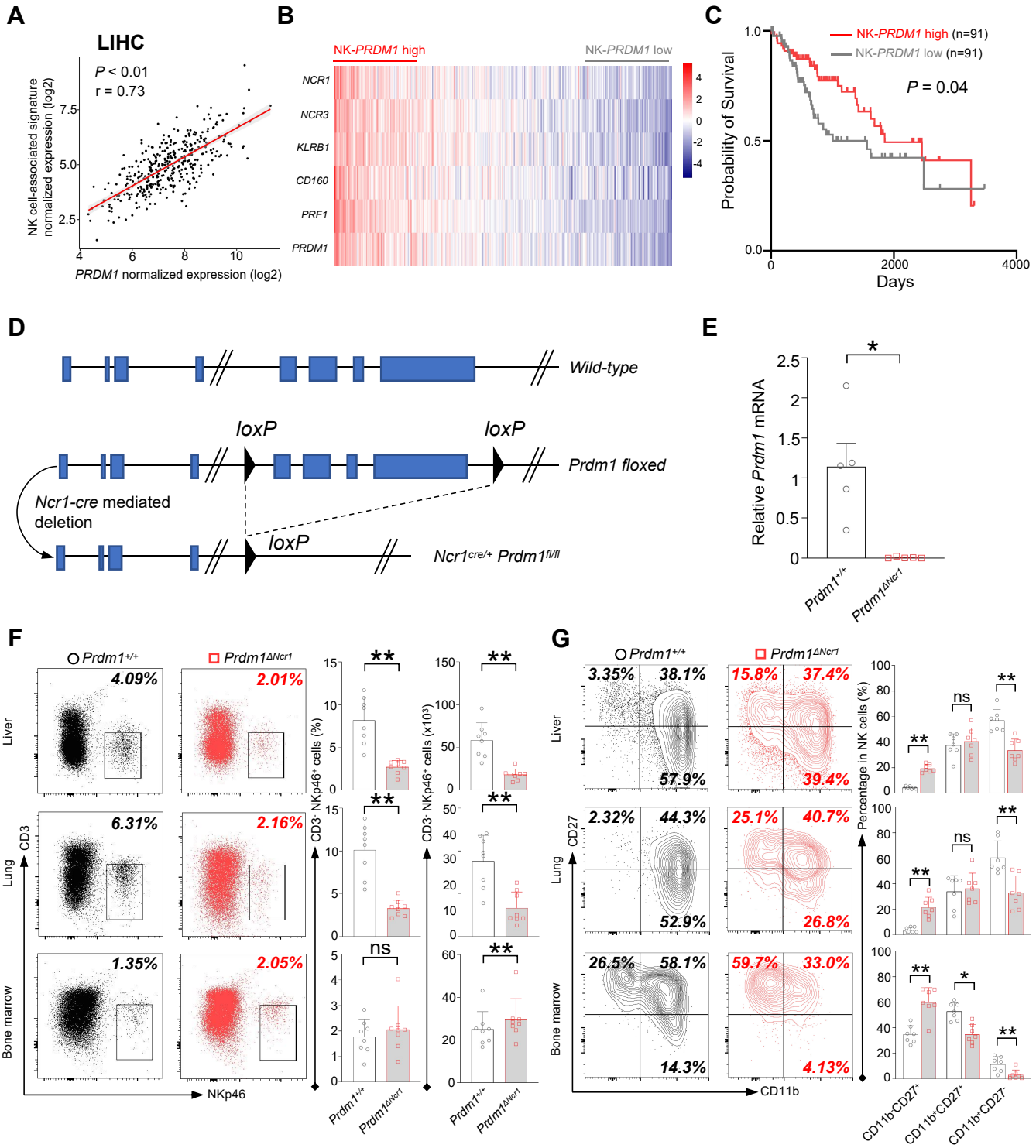

Figure 1. *Prdm1* promotes type I ILCs homeostasis and terminal maturation.
(**A**) Correlation between the average expression of NK cell-associated genes(*NCR1*, *NCR3*, *PRF1*, *CD160*, *KLRB1*) and *PRDM1* in LIHC (Liver Hepatocellular Carcinoma; n=363) patients sourced from TCGA datasets. (**B**) Heatmap of the ordered, z-score normalized expression values for *PRDM1* and NK cell-associated genes in liver cancer patients. The top and bottom quartiles of all patient samples are indicated. (**C**) Prognostic value of the *NK-PRDM1* signature for overall survival of liver cancer patients comparing high and low quartiles. (**D**) Schematic representation of the Prdm1-conditional knockout mouse model. Targeted exon 6-8 of *Prdm1* (top) is flanked with *loxP* sites (middle). Ncr1-expressed Cre recombinase was used to generate the *Prdm1*$^{\Delta Ncr1}$ allele (bottom). (**E**) Real-time RT-PCR quantification of *Prdm1* expression in NKp46^{+} cells to determine the presence of *Prdm1* (n=5). (**F**) Representative flow cytometric plots (left) and quantification (right) of the proportion and absolute number of CD3^{-}NKp46^{+} cells among lymphocytes in liver, lung, and bone marrow (n=8). (**G**) Representative flow cytometric plots (left) of the CD11b and CD27 expression within CD3^{-}NK1.1^{+}NKp46^{+} cells in liver, lung, and bone marrow (n=7). Right panel showed the percentage of distinct stages of NK cells. Data are presented as the mean±SEM and were analyzed by 2-tailed, paired t-test. Differences were evaluated between littermates. Each circle and square on graphs represents an individual mouse; *P*, *P*-value; r, pearson correlation coefficient; *, *P*<0.05; **, *P*<0.01, ns, not significant.

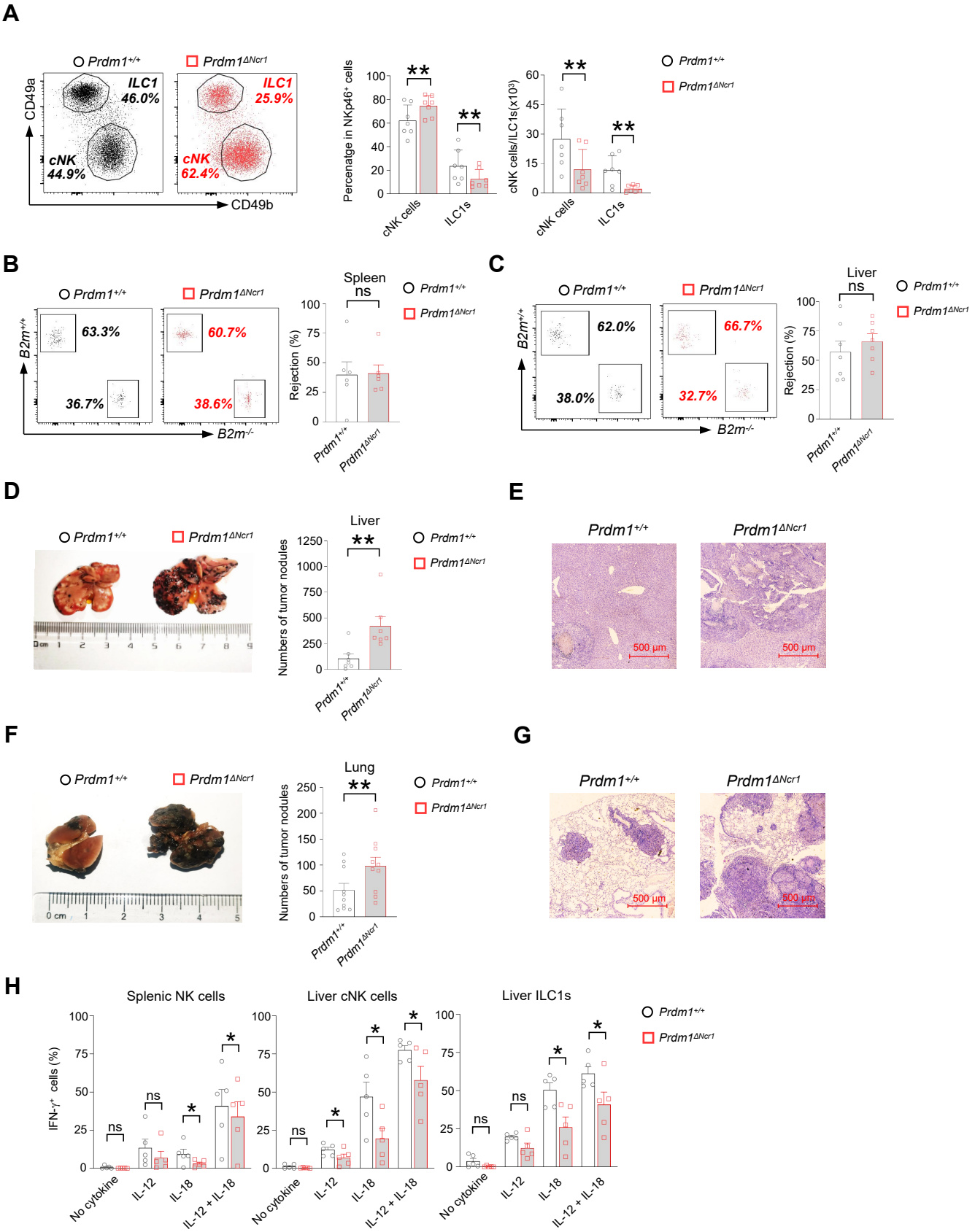

Figure 2. *Prdm1* is required for type I ILCs to control tumor metastasis.
(**A**) Representative flow cytometric plots (left) of liver cNK cells (CD49a$^-$CD49b$^+$) and ILC1s (CD49a$^+$CD49b$^-$) from *Prdm1*$^{+/+}$ and *Prdm1*$^{\Delta Ncr1}$ mice. The two bar graghs (right) quantitate the percentages and absolute numbers of cells respectively (n=7). (**B** and **C**) Splenocytes from *B2m*$^{-/-}$ and *B2m*$^{+/+}$ were labeled with CFDASE and eF670 respectively. Labeled cells were 1:1 mixed and injected i.v. into *Prdm1*$^{+/+}$ and *Prdm1*$^{\Delta Ncr1}$ recipient mice to evaluate *in vivo* NK cell target-killing ability. Representative flow cytometric plots (left) of transferred cells recovered from recipient mice and percentage (right) of NK cell-specific rejection of donor cells in spleen (n=6) (**B**) and liver (n=7) (**C**) between *Prdm1*$^{+/+}$ and *Prdm1*$^{\Delta Ncr1}$ mice. (**D** and **F**) Image (left) and quantification (right) of tumor nodes on the livers (n=7) (**D**) and lungs (n=10) (**F**) of *Prdm1*$^{+/+}$ and *Prdm1*$^{\Delta Ncr1}$ mice at day 14 or 21 after inoculation with B16F10 melanoma cells. (**E** and **G**) Histopathological images of liver (**E**) and lung (**G**) tissues stained by hematoxylin-eosin to detect tumor metastasis. Red bar indicates 500 μm distance under the microscope. (**H**) Liver cells and splenocytes were costimulated in the presence or absence of IL-12 and IL-18 for 12 hours. GolgiStop was added 4 hours before intracellular staining of IFN-γ. The graphs showed percentage of IFN-γ$^+$ splenic cNK cells, liver cNK cells and ILC1s from *Prdm1*$^{+/+}$ and *Prdm1*$^{\Delta Ncr1}$ mice (n=5). Data are presented as the mean±SEM and were analyzed by 2-tailed, paired t-test. Differences were evaluated between littermates. Each circle and square on graphs represents an individual mouse; *P*, *P*-value; *, *P*<0.05; **, *P*<0.01, ns, not significant.

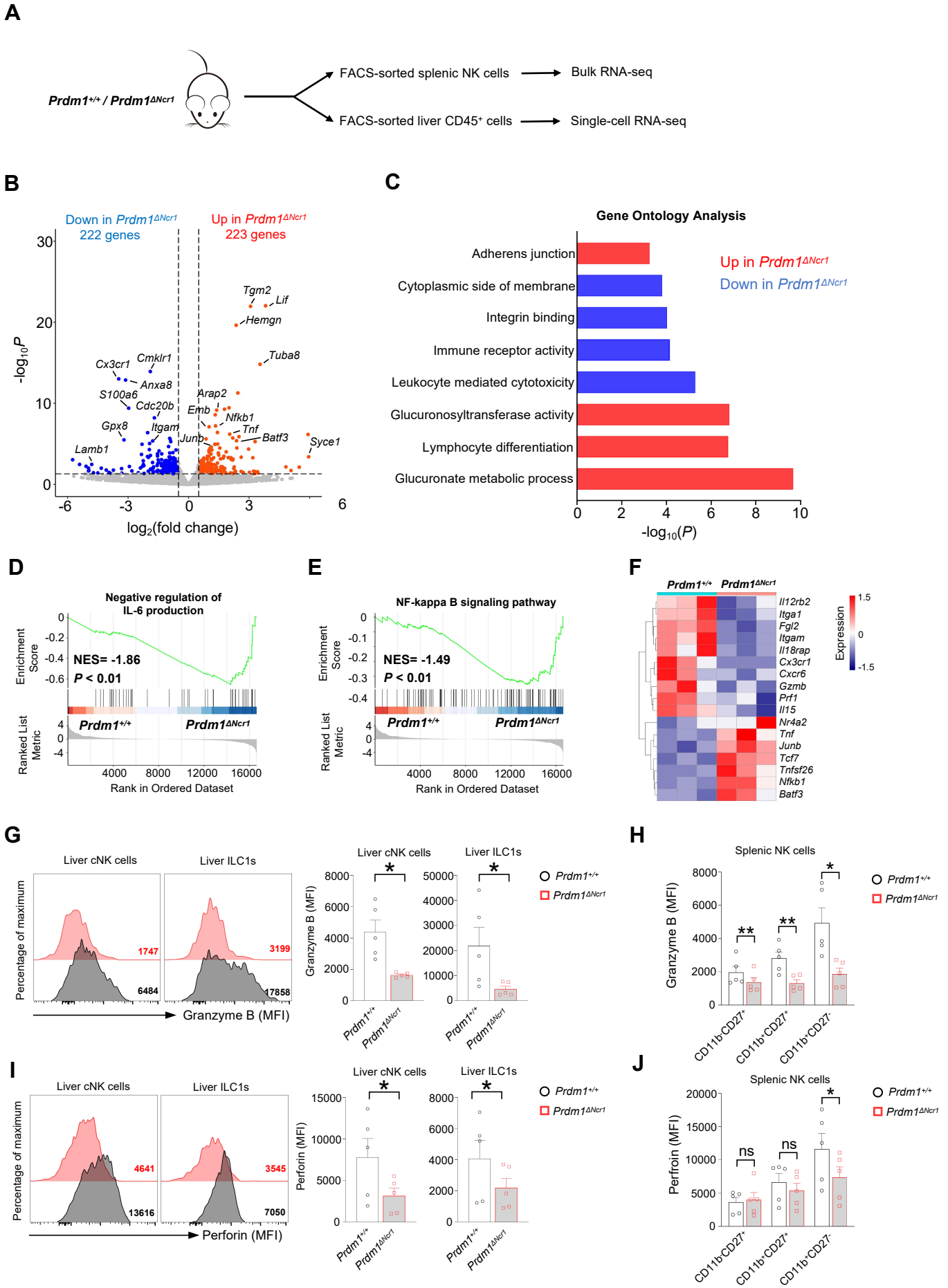

Figure 3. Bulk RNA-seq depicts *Prdm1*-mediated functions in peripheral cNK cells.
(**A**) Splenic cNK cells and liver CD45$^+$ cells were sorted from *Prdm1*$^{+/+}$ and *Prdm1*$^{\Delta Ncr1}$ mice using flow cytometry, and prepared for bulk RNA-seq and single-cell RNA-seq analysis. (**B**) Volcano plot of the bulk RNA-seq differentially expressed genes ($\log_2$(fold change)>0.5; P<0.05) in splenic cNK cells between *Prdm1*$^{+/+}$ and *Prdm1*$^{\Delta Ncr1}$ mice. Upregulated and downregulated genes in *Prdm1*$^{\Delta Ncr1}$ cells were highlighted in red and blue. (**C**) Enriched Gene Ontology (GO) terms of DEGs in *Prdm1*$^{\Delta Ncr1}$ cells compared *Prdm1*$^{+/+}$ cells. The Enrichment gene set in upregulated (red) and downregulated (blue) genes were indicated in different colours. Bar length represents statistical significance. (**D** and **E**) Gene Set Enrichment Analysis (GSEA) showing the enrichment of negative regulation of IL-6 production (**D**) and NF-kappa B signaling pathway (**E**) of DEGs in *Prdm1*$^{\Delta Ncr1}$ cells compared *Prdm1*$^{+/+}$ cells. NES, normalized enrichment score. (**F**) Heatmap of selected genes from DEGs. Shown is z-score transformed expression of DEGs. (**G** and **I**) Representative flow cytometric plots (left) and cumulative data (right) showing the relative mean fluorescence intensities (MFIs) of Granzyme B (**G**) and Perforin (**I**) in liver cNK cells and ILC1s from *Prdm1*$^{+/+}$ and *Prdm1*$^{\Delta Ncr1}$ mice (n=5). (**H** and **J**) Relative MFIs of Granzyme B (**G**) and Perforin (**I**) in splenic NK cells at different stages of maturation was analyzed by flow cytometry (n=5). Data are presented as the mean±SEM and were analyzed by 2-tailed, paired t-test. Differences were evaluated between littermates. Each circle and square on graphs represents an individual mouse; P, P-value; *, P<0.05; **, P<0.01, ns, not significant.

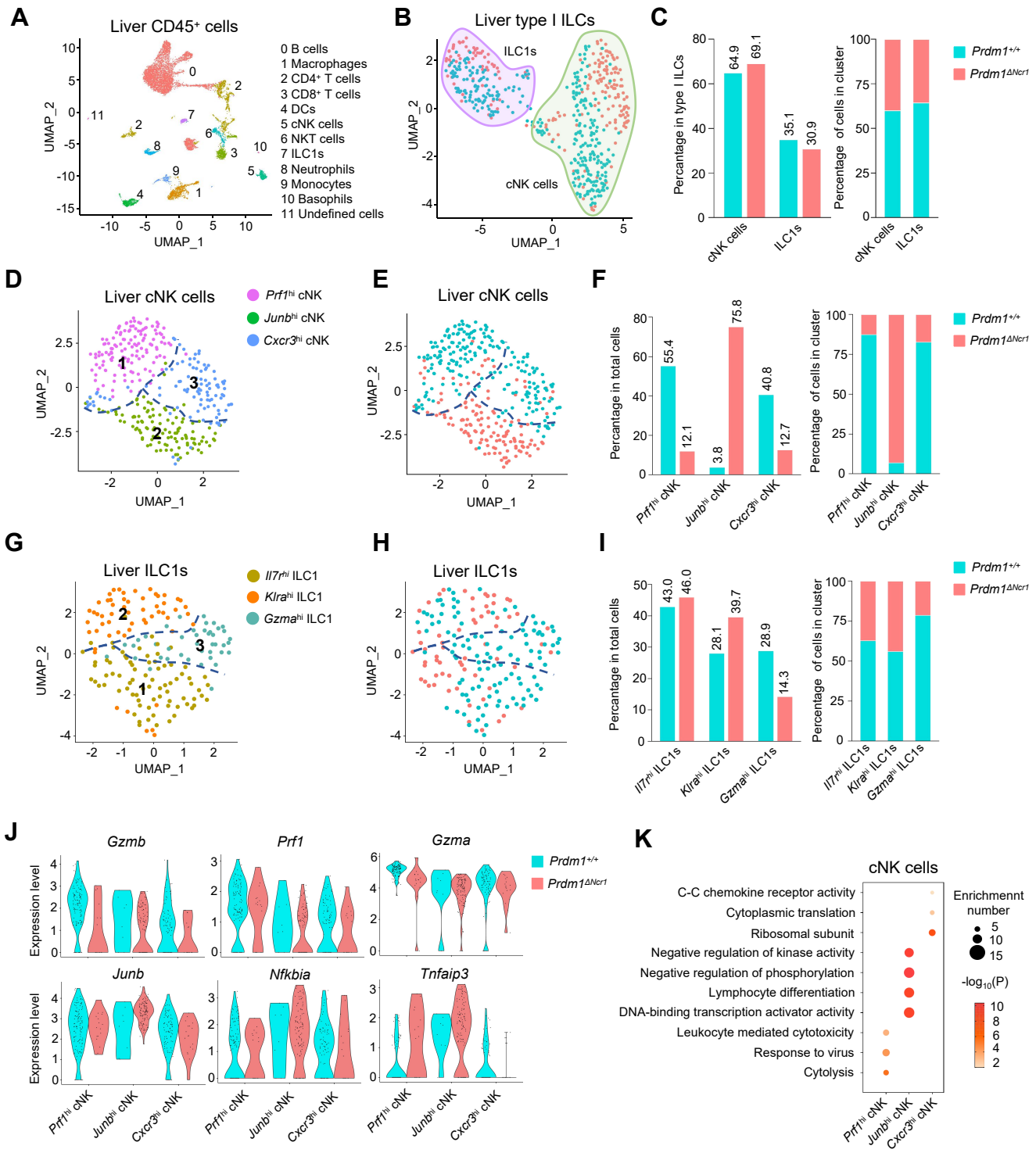

Figure 4. scRNA-seq reveals unique properties of two clusters from liver type I ILCs following *Prdm1* knockout.
(**A**) Uniform manifold approximation and projection (UMAP) visualization of liver CD45⁺ cells from *Prdm1*$^{+/+}$ and *Prdm1*$^{\Delta Ncr1}$ mice. Twelve clusters were defined and indicated by distinct colours. Each dot represents a single cell. (**B**) UMAP visualization of liver cNK and ILC1 clusters. Cells were colored by origins (*Prdm1*$^{+/+}$-blue; *Prdm1*$^{\Delta Ncr1}$-red). (**C**) Percentages of cNK cells and ILC1s in type I ILCs (left), and their distribution in each cluster (right). (**D-I**) UMAP visualization of three different liver cNK (**D**) and ILC1 (**G**) clusters from two mouse strains (**E** and **H**). Proportions of cNK cells (**F**) and ILC1s (**I**) among total cells (cNK cells or ILC1s) (left) and within clusters (right) were calculated respectively. (**J**) Violin plots showing the normalized expression of select genes in different cNK clusters. (**K**) Enriched GO term of marker genes in three cNK clusters. Dot size represents enriched gene number, and color intensity represents significance.

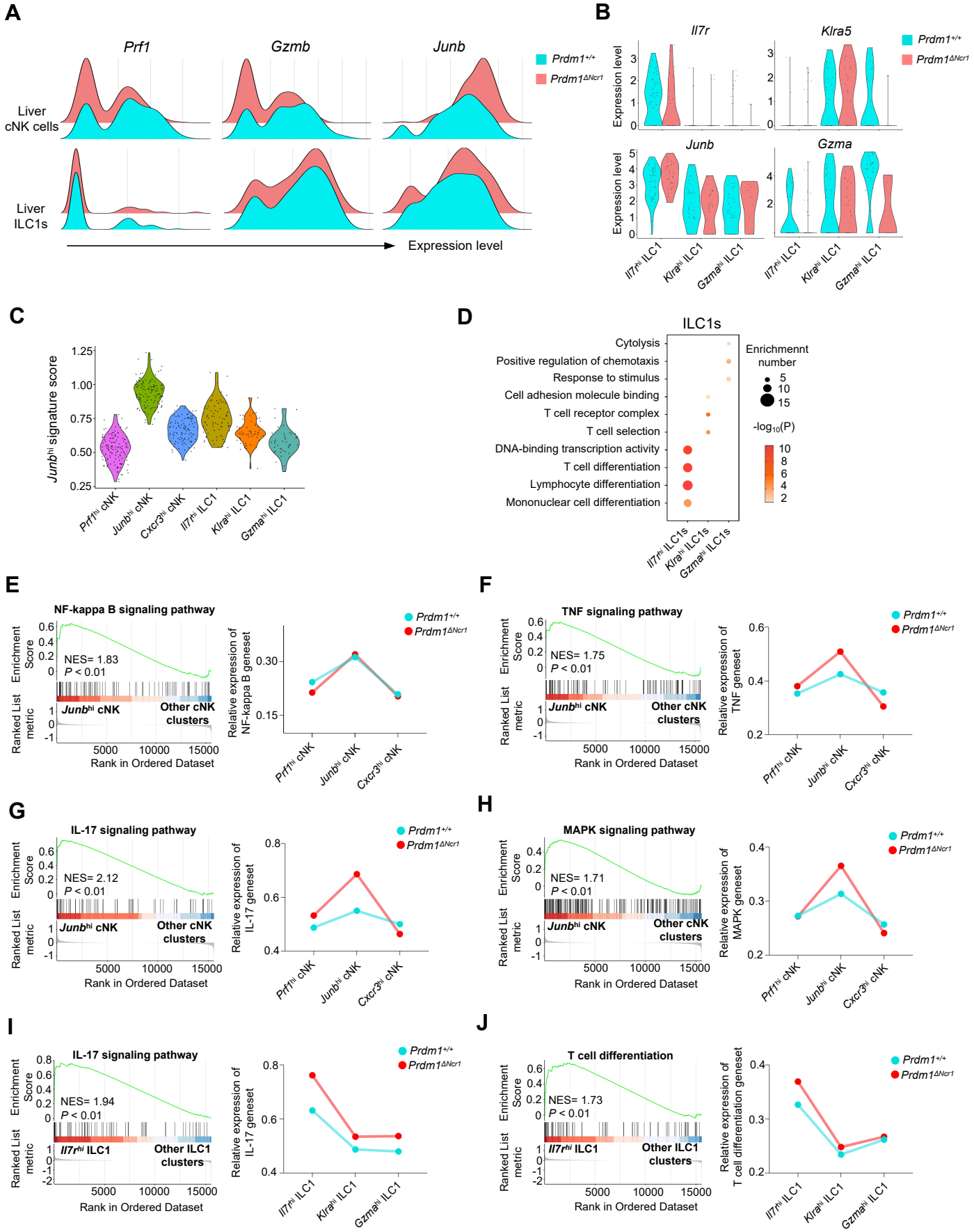

Figure 5. *Junb*^{hi} signature is associated with the activation of multiple signaling pathways.
(**A**) Ridge plots showing the normalized expression of *Gzmb, Prf1*, and *Junb* in cNK and ILC1 clusters between *Prdm1*$^{+/+}$ and *Prdm1*$^{\Delta Ncr1}$ cells. (**B**) Violin plots showing the normalized expression of select genes in different ILC1 clusters. (**C**) Violin plot showing the *Junb*^{hi} signature score for cNK cell and ILC1 clusters, calculated using the signature genes of *Junb*^{hi} cNK cluster. (**D**) Enriched GO term of marker genes in three ILC1 clusters. Dot size represents enriched gene number, and color intensity represents significance. (**E-J**) GSEA plots (left) depicting the enrichment of NF-kappa B (**E**) , TNF (**F**) , IL-17 (**G**) , and MAPK (**H**) signaling pathway in *Junb*^{hi} cNK cluster compared with clusters of *Prf1*^{hi} and *Cxcr3*^{hi} cNK cells, and the enrichment of IL-17 signaling pathway (**I**) and T cell differentiation (**J**) in *Il7r*^{hi} ILC1 cluster compared with clusters of *Klra*^{hi} and *Gzma*^{hi} ILC1s. Right panel showed dynamic relative expression of the given gene sets from cluster1 to cluster3 between *Prdm1*$^{+/+}$ and *Prdm1*$^{\Delta Ncr1}$. Dots represent the average expression of given gene set in each cell, which was calculated through the sum of normalized expression of each individual gene within the designated gene set in every single cell. NES, normalized enrichment score.

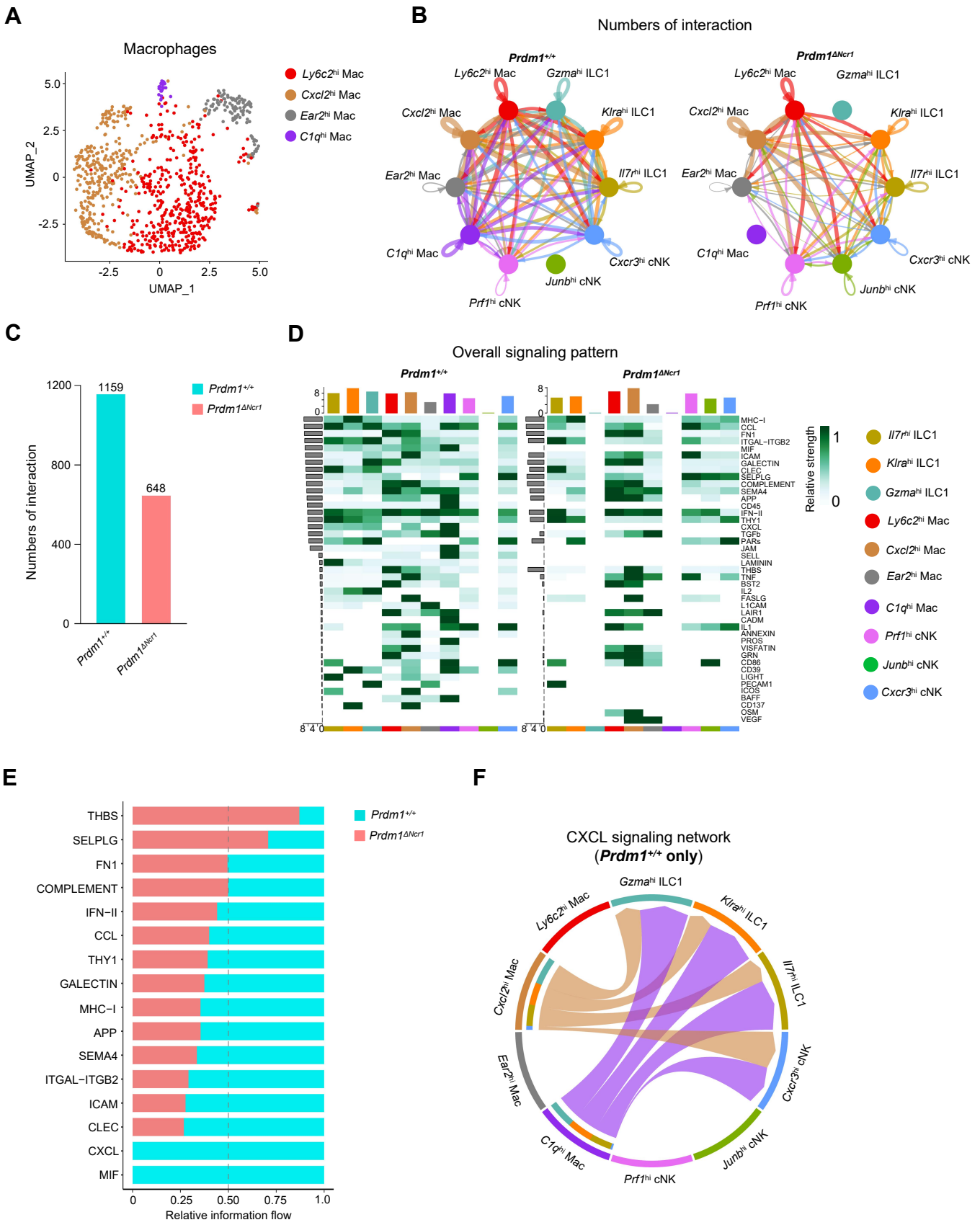

Figure 6. *Prdm1* facilitates the intercellular communication between liver type I ILCs and macrophages.
(**A**) UMAP visualization of macrophages (Mac) cluster. Four cell subsets were defined. (**B** and **C**) Circle plots (**B**) and summary data (**C**) illustrating the significant enriched ligand–receptor pairs among cluster of liver cNK cells, ILC1s, and macrophages from *Prdm1*$^{+/+}$ (left) and *Prdm1*$^{\Delta Ncr1}$ (right) cells. The thickness of the line indicates the number of enrich pairs, and the arrow reflects the direction of the interaction. (**D**) Heatmap of overall signaling pattern recognized from ligand-receptor pairs, which contained the sum of signaling from the sender and target cells. (**E**) Bar graphs showing the information flow in selected active signaling patterns between *Prdm1*$^{+/+}$ and *Prdm1*$^{\Delta Ncr1}$ cells. Relative information flow was calculated as the sum of the communication probability in given signaling patterns. (**F**) Chord plot of the CXCL signaling interaction network among cluster of liver cNK cells, ILC1s, and macrophages in *Prdm1*$^{+/+}$ cells.

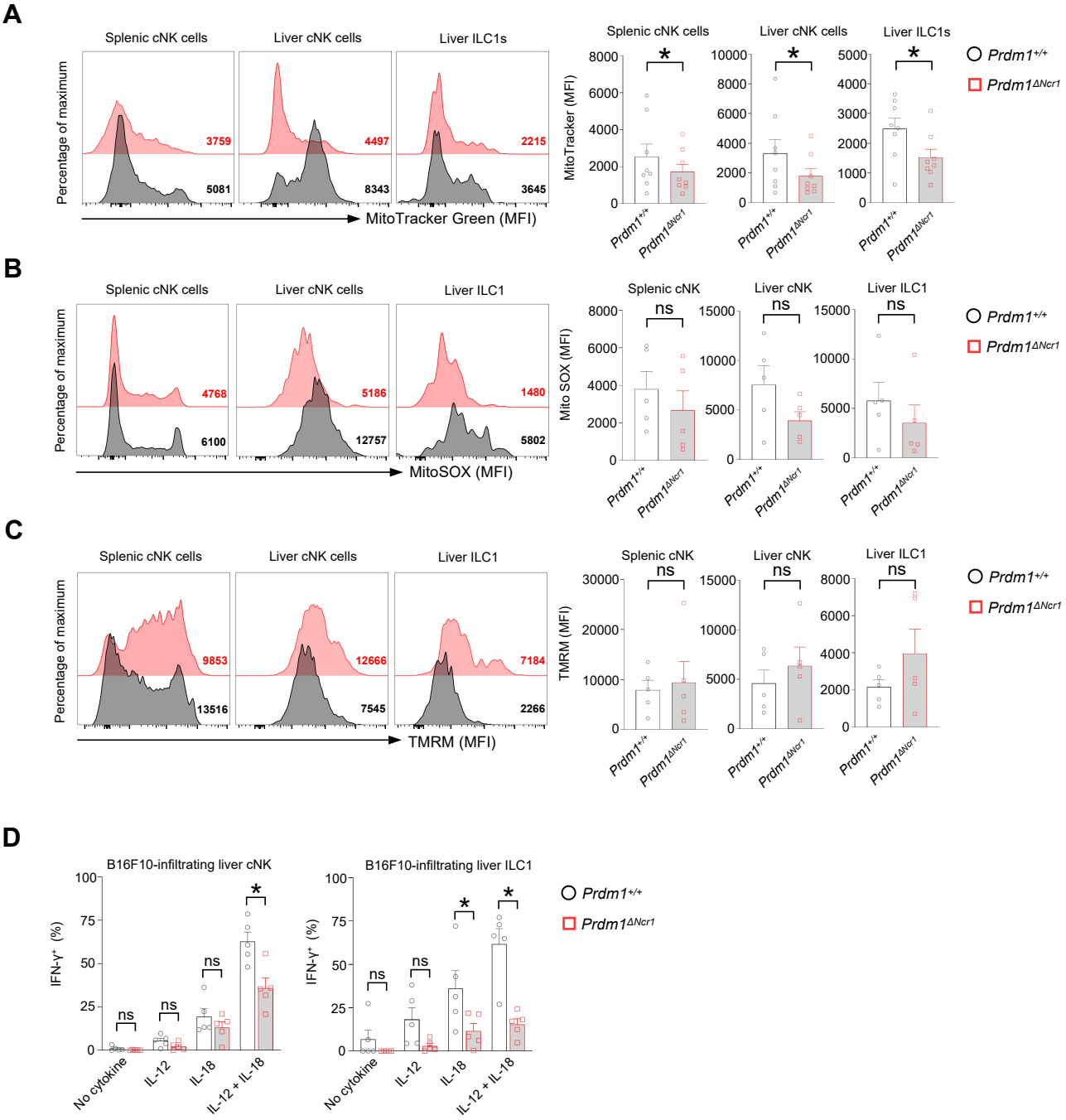

Figure 7. *Prdm1* safeguards type I ILCs from exhaustion-like phenotypes in the tumor microenvironment.
(A-C) The Mitochondrial mass (MitoTracker Green staining; n=8) (**A**), Mitochondrial ROS (MitoSOX staining; n=5) (**B**), and Mitochondrial membrane potential (TMRM staining; n=5) (**C**) of splenic cNK cells, liver cNK cells and ILC1s were analyzed by flow cytometry. Representative flow cytometric plots (left) and cumulative data (right) showing the relative mean fluorescence intensities (MFIs) of each group. (**D**) Percentages of IFN-γ^{+} liver cNK cells and ILC1s from *Prdm1*$^{+/+}$ and *Prdm1*$^{\Delta Ncr1}$ tumor-bearing mice at day 14 after inoculation with B16F10 melanoma cells via intrasplenic injection (n=5). Data are presented as the mean±SEM and were analyzed by 2-tailed, paired t-test. Differences were evaluated between littermates. Each circle and square on graphs represents an individual mouse; *P*, *P*-value; *, *P*<0.05; **, *P*<0.01, ns, not significant.